

# Clear sky atmosphere at cm-wavelengths from climatology data

Bartosz Lew,<sup>1\*</sup> Joanna Uscka-Kowalkowska,<sup>2</sup>

<sup>1</sup>*Toruń Centre for Astronomy, Nicolaus Copernicus University, ul. Gagarina 11, 87-100 Toruń, Poland*

<sup>2</sup>*Department of Meteorology and Climatology, Nicolaus Copernicus University, Lwowska 1, 87-100 Toruń, Poland*

Accepted 2015 October 28. Received 2015 October 08; in original form 2015 July 02

## ABSTRACT

We utilise ground-based, balloon-borne and satellite climatology data to reconstruct site and season-dependent vertical profiles of precipitable water vapour (PWV). We use these profiles to solve radiative transfer through the atmosphere, and derive atmospheric brightness temperature ( $T_{\text{atm}}$ ) and optical depth ( $\tau$ ) at centimetre wavelengths.

We validate the reconstruction by comparing the model column PWV with photometric measurements of PWV, performed in clear sky conditions pointed towards the Sun. Based on the measurements, we devise a selection criteria to filter the climatology data to match the PWV levels to the expectations of the clear sky conditions.

We apply the reconstruction to the location of a Polish 32-metre radio telescope, and characterise  $T_{\text{atm}}$  and  $\tau$  year-round, at selected frequencies. We also derive the zenith distance dependence for these parameters, and discuss the shortcomings of using planar, single-layer, and optically thin atmospheric models in continuum radio-source flux-density measurement calibrations.

We obtain PWV- $T_{\text{atm}}$  and PWV- $\tau$  scaling relations in clear sky conditions, and constrain limits to which the actual  $T_{\text{atm}}$  and  $\tau$  can deviate from those derived solely from the climatological data.

Finally, we suggest a statistical method to detect clear sky that involves ground-level measurements of relative humidity. Accuracy is tested using local climatological data. The method may be useful to constrain cloud cover in cases when no other (and more robust) climatological data are available.

**Key words:** radiative transfer – atmospheric effects – site testing – radio continuum: general – methods: observational

## 1 INTRODUCTION

Ground-based, cm-wavelengths radio continuum observations of astrophysical sources depend on atmospheric emission, and absorption of the incident radiation. Time varying line-of-sight (LOS) abundance of ice, liquid water, and water vapour generates variable optical depth, which leads to signal instabilities. These instabilities do not average out under long integrations due to the steep spectrum of turbulent atmospheric water density fluctuations. The atmospheric effects associated with dry air thermal emission, continuum and line absorption are frequency-dependent, and can be characterised by atmospheric brightness temperature ( $T_{\text{atm}}(\nu)$ ) and transmittance ( $t_{\text{atm}}(\nu)$ ). These atmospheric emissions contribute to the system temperature ( $T_{\text{sys}}$ ) that

limits the sensitivity of any ground-based telescope-receiver pair.

Over the last few decades, monitoring temperature, pressure, density, and other altitude dependent parameters of air, have helped to develop a few widely-accepted models of Earth’s atmosphere. Advances in atomic and molecular line spectroscopy provided absorption coefficients for various gas species, and computer-generated spectra for mixtures of gases under given thermodynamic conditions can now reproduce these observations in great detail. Thus, the radiative properties of the atmosphere are well known, and can be derived from the first principles, from radio waves to infrared frequencies.

At cm-wavelengths the electromagnetic spectrum of  $T_{\text{atm}}$  is predominantly defined by continuum absorption, and emission of oxygen ( $\text{O}_2$ ) and water vapour ( $\text{H}_2\text{O}$ ) molecules. The latter results from strong coupling of the electric dipole moment of water molecules to the millimetre radiation via

\* E-mail: blew@astro.uni.torun.pl

rotational transitions. Going to liquid and ice states less and no rotational freedom is possible respectively, and therefore droplets and ice particles are expected to radiate less per molecule. In the presence of clouds, the background signals are additionally attenuated in ice and droplets, decreasing the signal-to-noise ratio (SNR) of any radio source. This translates to an increased observational time required to detect the same source at the same significance level, as compared to the situation without clouds. Given that the cloud cover is non-uniform and variable, the amount of the attenuation will change over time, generating variance at different time scales in the signal received through the main beam, or through side-lobes. For the radio continuum flux density observations at cm- and mm-wavelengths, this means that nearly clear sky conditions are required, although in practice, observations are also viable when some high-level icy clouds are present.

Unlike the 'dry' component of air, the distribution of atmospheric water on Earth is strongly dependent on location. For this reason many dedicated radio telescopes are built at high altitudes and in dry and/or cold climates (such as the Atacama desert or the South Pole). This reduces atmospheric emissions, maximises transmittance, improves thermal stability, and rules out cloud attenuation. At other locations, atmospheric water variations must be monitored to optimally match the observational programme to the current weather conditions. In clear sky conditions, measurements of precipitable water vapour (PWV) can be useful in working out optical depths and estimating atmospheric absorption corrections of astronomical radio source flux density measurements.

Atmospheric water vapour can be measured in a number of ways, including (i) radio sounding, (ii) atmospheric delays of GPS-satellite signals, (iii) sun photometry of water lines in near-infrared light, (iv) direct radiometric measurements in water bands (e.g. Liljegren et al. (2001)). In the larger time scales, PWV can be modelled statistically using climatological data.

Currently, the publicly-available data from ground-based meteorological stations, radio sounding, and satellite observations allow reconstruction of the vertical structure of atmosphere at particular locations of interest. For example, the Integrated Global Radiosonde Archive (IGRA) data, which we use in this analysis, provides substantial aerial coverage and density worldwide, but only a few atmospheric parameters are measured at relatively large time intervals (only twice a day). Likewise, many satellite data obtained with the solar occultation method also have nearly global coverage, but their sensitivity is largely limited in the troposphere due to clouds. However, these meteorological data can be used to model the total average PWV on a month-by-month basis. Whether by direct radiometric observations or by solving radiative transfer equations, many radio astronomical observation sites have  $T_{\text{atm}}$  and  $t_{\text{atm}}$  calculated at the desired frequencies and the time of year (Ajello et al. 1995; Radford & Holdaway 1998; Bussmann et al. 2005; Bustos et al. 2014). In this paper we will characterise the atmosphere in these terms for the first time for the location of the 32-metre radio telescope (RT32) in Poland, and show that a similar approach can be easily adapted to virtually any other location. The RT32 is one of the European VLBI Network stations, currently capable of

observations in the L, C, K and Ka frequency bands (see Lew et al. (2015) for more RT32 specifications).

The motivation for investigating local atmosphere arises from the planned radio source survey with the 30-GHz OCRA-f focal plane, 4-pair, beam-switched receiver (Lew et al. 2015). In particular, we seek to improve the atmospheric model, previously used for the continuum flux density measurement calibrations (Gawroński et al. 2010; Peel 2010; Lancaster et al. 2011), which requires estimates of the atmospheric optical depth ( $\tau$ ) at the source zenith distance ( $z_d$ ). These estimates are typically obtained by performing tipping scans, with the assumption that  $T_{\text{atm}}(z_d) \approx T_{\text{atm}}(0) \sec(z_d)$ . We investigate the limits of validity of this, and other approximations, using radiative transfer in the atmosphere in clear sky conditions.

Radio sounding and satellite data are recorded independently of weather conditions, and modelling PWV in clear skies requires employing selection criteria that would assure that the filtered subset of the data corresponds to the clear sky conditions at a particular location and observation time. A search for such selection criteria, given the aforementioned sparsity and deficiencies of the sounding data, is also one of the aims of this paper.

The structure of this paper is as follows. In section 2 we discuss the publicly available climatological data used in our reconstructions of atmospheric profiles, describe the atmospheric model parametrisation and introduce our PWV measurements. In section 3 we describe the radiative transfer approach to calculating atmospheric transmittances and brightness temperatures. The main results are gathered in Sec. 4. Discussion and conclusions are in sections 5 and 6 respectively.

## 2 DATA

We consider contributions to  $T_{\text{atm}}$  and  $t_{\text{atm}}$  from dry air (with standard nitrogen to oxygen proportions), ozone ( $O_3$ ) and water vapour ( $H_2O$ ), and ignore atmospheric trace gases. In the following subsections, we describe the climatological data, used to reconstruct a localised, vertical structure of the atmosphere, which is a starting point for radiative transfer.

### 2.1 Vertical pressure and temperature profiles

We reconstruct vertical atmospheric temperature and pressure profiles using the COSPAR<sup>1</sup> International Reference Atmosphere project data<sup>2</sup> (hereafter CIRA86) (Rees 1988; Rees et al. 1990; Rees 1992). These zonally-averaged data are a compilation of ground-based, radiosonde and satellite measurements of atmospheric pressure, temperature, wind velocity and geopotential height up to an altitude of  $z = 120$  km, with  $5^\circ$  latitude resolution, roughly 2 km vertical resolution, and nearly global coverage in latitudes ( $\theta = [80^\circ\text{S}, 80^\circ\text{N}]$ ). We use the monthly averaged vertical profiles of pressure  $P(z_g)$  and temperature  $T(z_g)$ , given as a

<sup>1</sup> Committee on Space Research

<sup>2</sup> <http://badc.nerc.ac.uk/data/cira>

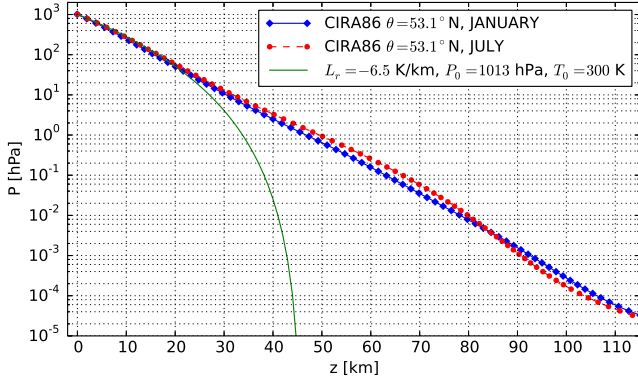


**Figure 1.** Atmospheric pressure profiles in January (solid, blue) and in July (dashed, red) interpolated from the CIRA86 data for the latitude  $\theta_T = 53.1^\circ\text{N}$ . For comparison, the theoretical profile (Eq. 1) is plotted for the assumed values of lapse-rate ( $L_r$ ), pressure ( $P_0$ ), and temperature ( $T_0$ ) (bottom solid-green curve).

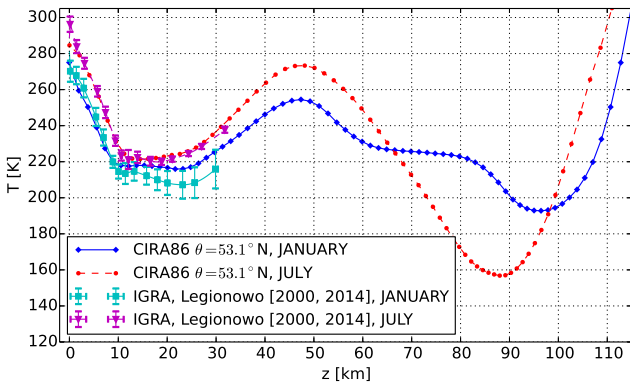


**Figure 2.** Atmospheric temperature profiles in January (solid, blue) and in July (dashed, red) interpolated from the CIRA86 data for the latitude  $\theta_T = 53.1^\circ\text{N}$ . The curves extending up to  $z \approx 30$  km are the IGRA radiosonde data from Legionowo station, averaged over the period of 15 years. The horizontal error bars represent  $\pm 1\sigma$  dispersion resulting from variable geopotential altitudes assigned to the fixed pressure levels. The vertical error bars represent  $\pm 1\sigma$  dispersion of temperatures in the selected month.

function of geopotential height and we apply an interpolation to obtain a profile for the desired latitude. Throughout this paper we will interpolate the profiles for the latitude  $\theta_T = 53.1^\circ\text{N}$  – the latitude of the Toruń Centre for Astronomy (TCfA). Geopotential height ( $z_g$ ) is related to geometrical height ( $z$ ) above the sea level via:  $z_g = z R_\oplus / (R_\oplus + z)$ , where  $R_\oplus = 6371$  km is the assumed value of Earth radius. In what follows, we will ignore the difference between the two heights, as they are almost identical over the range of altitudes of interest. The differences are also unimportant when compared to the variance generated by weather related pressure variations. Associating the fixed CIRA86 pressure levels to altitudes ( $z$ ) allows us to assign geometrical heights to other physical quantities of interest as well, such as temperature, relative humidity, and mixing ratios, which are typically recorded at fixed pressure levels.

The interpolated CIRA86 pressure profiles are shown in Fig. 1. For visualisation we compare them against the theoretical model with the altitude-independent lapse rate (NASA 1976):

$$P(z) = P_0 \left[ \frac{T_0}{T_0 + L_r(z - z_0)} \right]^{\frac{g_0 \mu}{R L_r}} \quad (1)$$

where  $L_r$  is the lapse rate (Fig. 1), where  $g_0 = 9.80665$  km/s<sup>2</sup> is the assumed surface acceleration of the Earth,  $R = 8.31432$  J · mol<sup>-1</sup> · K<sup>-1</sup> is the gas constant,  $\mu = 0.0289644$  kg · mol<sup>-1</sup> is the molar mass of the air and  $P_0$ ,  $T_0$  and  $z_0$  are fiducial pressure, temperature and altitude respectively. While the consistency is very good in the troposphere, the deviation from the measured profiles in the stratosphere results from the lapse rate increasing to zero as one approaches tropopause, the fact that we do not take into account in this visualisation.

In order to adjust the pressure profiles to the local conditions and improve the reconstruction at low altitudes ( $z \lesssim 13$  km), we combine CIRA86 profile with the profile extracted from the local sounding data (see section 2.2.1). However, the two profiles turn out to be quite compatible, with the biggest discrepancy of  $\sim 8\%$  at  $z = 30$  km in January, and much smaller in July.

Similarly, in the case of temperature profiles, we gauge the impact of the longitudinal deviations from the CIRA86 mean, by comparing it with the daytime radio sounding profile from Legionowo (near Warsaw, Poland), averaged over the period 2000-2014. We find the two datasets consistent to within 8% in the stratosphere and in the lower troposphere (Fig. 2). The consistency is better between the two regimes. The near-ground departures from the zonal averages are somewhat expected, which is why we rely on the sounding data at low altitudes. The two datasets clearly mark the transition to tropopause at an altitude of about 10 km at the considered latitude.

## 2.2 Vertical WV profiles

### 2.2.1 Relative Humidity profiles

Of all trace atmospheric gases, WV is of the greatest relevance for the cm-wavelength observations. WV volume mixing ratio (VMR) — the number density of H<sub>2</sub>O molecules relative to number density of all other species in the atmosphere — is highest in the troposphere. At these altitudes satellite data are no longer useful, and WV mixing ratios or alternatively the relative humidity (RH) for a given pressure and temperature, must be estimated from radio sounding data. The data is publicly available from the Integrated Global Radiosonde Archive<sup>3</sup> (Durre et al. 2006) updated on daily basis. There are several hundreds of stations around the globe, allowing vertical profiles reconstruction with the land surface spatial resolution of the order of a few hundred kilometres, on average. A typical radiosonde accuracy to perform the temperature, pressure and RH measurement is about 0.5 °C, 1 hPa, and 1% respectively (Peixoto & Oort 1996).

<sup>3</sup> <http://www1.ncdc.noaa.gov/pub/data/igra>

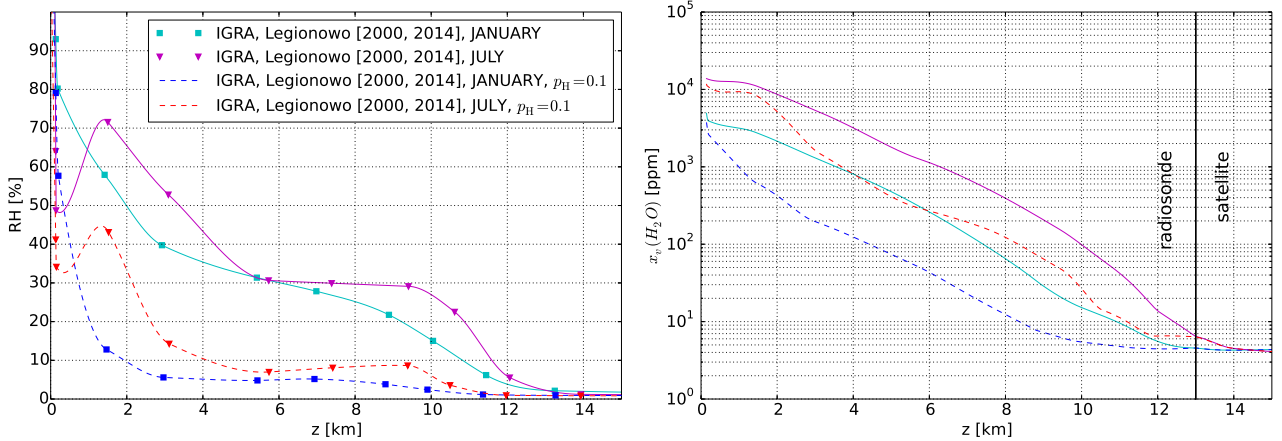


**Figure 3.** (Left) Monthly-average relative humidity profiles from the Legionowo IGRA station in January (triangles) and July (squares) for the case of unscreened data (solid), and for the subset of 10% driest conditions (dashed) as indicated by  $p_H = 0.1$  in the plot legend. (Right) Corresponding H<sub>2</sub>O volume mixing ratio profiles. The vertical line indicates transition altitude above which the satellite data is used. The satellite water abundances are not subject to the selection criterion.

For the purpose of our analysis we choose the radiosonde data from the Legionowo station located near Warsaw (Poland) as they have been archived since 1957. The data contain daily records of geopotential height ( $z_g$ ), temperature ( $T$ ), dew point depression ( $\Delta T_d \equiv T - T_d$ , where  $T_d$  is dew point temperature) wind direction, and wind speed, probed twice a day (midnight and noon) at fixed pressure levels ( $P_i$ ), as the radiosonde travels up the atmosphere. We will hereafter refer to this data as IGRA. For any given month we use the daily daytime records between and including the years 2000 and 2014. We reject the data that have incomplete or incorrect height, temperature or dew point depression information. This leaves a few thousand records per month for further analysis.

At each pressure level and for each  $\{T, P, T_d\}$  tuple we derive the corresponding relative humidity by analytically solving the following equation:

$$T_d(T, \text{RH}) = \frac{\lambda \Gamma(T, \text{RH})}{\beta - \Gamma(T, \text{RH})} \quad (2)$$

where

$$\Gamma(T, \text{RH}) = \ln\left(\frac{\text{RH}}{100}\right) + \frac{\beta T}{\lambda + T} \quad (3)$$

and  $T$  is in Celsius and RH is expressed as percentages (see e.g. Lawrence (2005) for the derivation). In Eq. 3 the constants are:  $\beta = 17.62$  and  $\lambda = 243.12^\circ\text{C}$  (Sonntag 1990). These values yield  $T_d$  consistent with a more rigorous derivation of Hardy (1998) to within  $0.3^\circ\text{C}$  for the temperature range from  $-50^\circ\text{C}$  to  $50^\circ\text{C}$ , and within the measured range of relative humidities. See also Alduchov & Eskridge (1997) to review the values of the constants from other studies.

We associate the RHs with altitudes using the reconstructed  $P(z)$  relation (Sec. 2.1), and employ Akima interpolation (Akima 1970) to create a tabulated version of the profiles. We use the sounding data up to  $z \sim 13$  km and satellite data at higher altitudes (Fig. 3). The near-ground tail of each RH profile is supplemented with the average RH data point recorded by the local meteorological station. This improves adjustment to the RT32 site conditions.

In order to create a low-humidity subset of the data –

conditions that typically correspond to a cloudless sky – we select the IGRA records according to the quantile function  $Q(p_H)$  of the RH record distribution, in each of the pressure levels independently (sec. 2.5). Thus  $p_H$  is a selection parameter, corresponding to the probability that a random observation at any pressure level will have the RH value smaller than  $Q(p_H)$ . In order to visualise the selection effect we arbitrarily choose  $p_H = 0.1$ , corresponding to the 10% driest conditions for the considered month in the year-to-year data samples (Fig. 3, dashed lines). We will later fine tune this choice using external data. The resulting yearly samples are averaged into a single profile that approximates the local climate for a given month.

We convert the reconstructed RH profiles into H<sub>2</sub>O VMR profiles ( $x_v(\text{H}_2\text{O})$ ) using the following formula:

$$x_v(\text{H}_2\text{O}) = \left(\frac{\text{RH}}{100}\right) \frac{P_{\text{sat}}(T)}{P} \quad (4)$$

where  $P$  is the total atmospheric pressure, and  $P_{\text{sat}}$  is the saturation pressure of water vapour at temperature  $T$ .  $P_{\text{sat}}$  is calculated using equation number 10 of Murphy & Koop (2005), reported to be valid within the range of temperatures considered in this paper. The reconstructed  $x_v(\text{H}_2\text{O})$  profiles are shown in Fig. 3 (right panel). At higher altitudes the profiles are reconstructed using satellite data.

A comparison of CIRA86 and Legionowo radiosonde data in terms of temperature shows that the two agree very well in the region of the upper troposphere (Fig. 2). However, there is a systematic dependence of the upper tropospheric RHs recorded by radiosondes in the period from 1979 to 1991, on geographical location. The dependence results from the type of instrumentation that has been used (Soden & Lanzante 1996). For this reason, in this analysis, we refrain from using data from the previous century, and rely on the data from the previous and current decades, as technology exchange it is likely to have mitigated these inconsistencies. Peixoto & Oort (1996) has also investigated radiosonde humidity data (recorded in the period from 1973 to 1988), performed cross-checks with SAGE satellite measurements, and found similar discrepancies as those pointed out by Soden & Lanzante (1996), but confirmed that in the

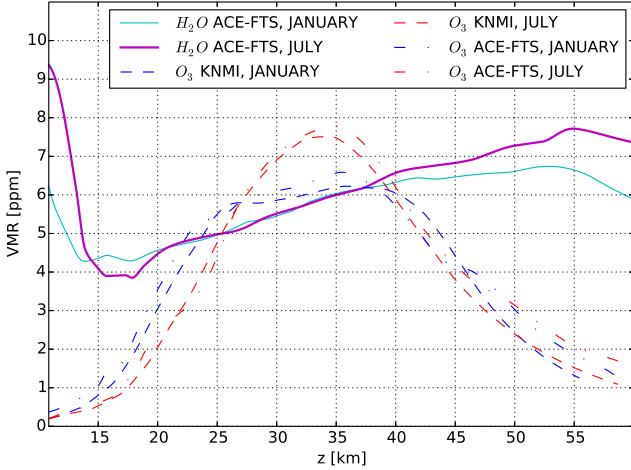


**Figure 4.** WV volume mixing ratio profiles (solid) interpolated at  $\theta_T = 53.1^\circ\text{N}$  from ACE-FTS data in January (cyan, thin) and July (magenta, thick). The dashed (dash-dotted) lines represent the ozone VMR profiles interpolated from the KNMI (ACE-FTS) data in January (blue) and July (red) (see Sec. 2.3).

lower and middle troposphere the discrepancies are not important.

### 2.2.2 Water Vapour mixing ratio profile

We use the data from the Fourier Transform Spectrometer (Jones et al. 2012) of the Atmospheric Chemistry Experiment<sup>4</sup> (ACE-FTS) (Bernath et al. 2005) in order to include the stratospheric water vapour.

The interpolated profile is shown in Fig. 4. We combine it with the tropospheric radiosonde profile using a linear transformation from one profile to another within the range of overlapping altitudes (typically  $10 \lesssim z \lesssim 13$  km). We verified, however, that the impact of the stratospheric WV is negligible and could be ignored in the case of ground-level sites.

## 2.3 Ozone

We model the local atmospheric ozone VMR profile using a combination of ozonesonde and satellite data<sup>5</sup> provided by the Royal Netherlands Meteorological Institute (hereafter KNMI). The KNMI ozone data are zonally averaged VMRs measured over 17 different latitudes from  $-80^\circ\text{S}$  to  $80^\circ\text{N}$ , and at 19 different pressure levels from 0.3 hPa to 1000 hPa. The data is compiled from 30 ozone stations and SBUV-SBUV/2 satellite observations, collected during the years 1980-1991 (Paul et al. 1998).

Currently, there is a wealth of ozone data from many satellites and from radiosondes (e.g. WOUDC (1961); Fioletov et al. (2002); Jones et al. (2012)) that continuously

monitor the ozone layer. In the current work, our main focus is on the cm-wavelengths, where the ozone impact is sub-dominant, but for the sake of completeness and accounting for possible extensions into higher frequencies, we include one of the available ozone datasets (KNMI) into the analysis. The consistency between the profiles obtained from various ozone experiments is shown in Fig. 4.

## 2.4 Ground-level meteorological data

We improve the adjustment of the atmospheric model to the local conditions at the ground-level by including data recorded by the IRDAM WST7000 meteorological station, installed on the roof of TCfA, near RT32. The data include temperatures, pressures, and relative humidities recorded at a high time resolution. We used the data covering a period that slightly exceeds 4 years i.e. from October 2010 to November 2014. In each month they contribute as a single data point in the RH profile (Fig. 3) at the altitude of TCfA, but also influence higher altitudes via smooth interpolation. We detect a systematic effect in this RH dataset, resulting from a progressive deterioration of the humidity sensor over time. The effect leads to an overestimation of the local RHs by  $< 4\%$  in the years 2011 and 2014 as compared to the values from 2012, and less than that in the year 2013.<sup>6</sup> In our analysis we ignore these systematic effects as they are thought to be unimportant.

## 2.5 Data selection criteria and model parametrisation

We are interested in deriving a localised, mean  $T_{\text{atm}}$  and  $t_{\text{atm}}$  as a function of month in clear sky conditions. Using an unfiltered data, discussed in Sec. 2.2.1 and Sec. 2.4, would lead to biased results because only a fraction of the data is obtained at the times when there is no cloud cover. The fraction of time with clear sky conditions, depends on the location and the time of year. In particular, in the lowlands surrounding the RT32 observing site the fraction of days with the mean daily cloud cover  $\leq 20\%$  ranges from  $\sim 9\%$  to  $\sim 11\%$ , on average (Woś 2010).

As discussed in Sec. 1, there is an anti-correlation between RH and solar irradiance, which could statistically hint on clear sky conditions, if one selects data by low, ground-level RHs. Observations indicate however, that during the cloudiest months such selection criterion returns a considerable false-positive rates, as discussed in Sec. 4.6. However, there is another complication regarding this selection scheme. The correlation between water vapour content at the ground level and that at higher altitudes is rather weak, or non-existent. Some correlation exists only between the neighbouring pressure levels in the lower troposphere. For this reason, the parametrisation of the selection criterion by low RHs at a single, fixed pressure level lacks a very desired feature: that the mean column PWV should decrease monotonically as one straightens the selection criterion.

<sup>4</sup> The Atmospheric Chemistry Experiment (ACE), also known as SCISAT, is a Canadian-led mission mainly supported by the Canadian Space Agency.

<sup>5</sup> [http://www.knmi.nl/research/climate\\_chemistry/Data/FKClmatology/](http://www.knmi.nl/research/climate_chemistry/Data/FKClmatology/)

<sup>6</sup> In the end of 2011 the station was renewed, hence in 2012 it provided the least biased readouts. Therefore, the previous and the following years are biased to a greater extent.

Since we are interested in an assessment of the brightness temperature in the conditions that are *statistically* compatible with a clear sky situation in terms of the column PWV content, we will filter the data coherently at all pressure levels. For a given month and year, we use only the IGRA records that yield

$$\text{RH} < Q_{\text{RH},i,j}(p_{\text{H}}), \quad (5)$$

where  $Q_{\text{RH},i,j}(p_{\text{H}})$  is the quantile function of the RH distribution at  $i$ 'th pressure level in  $j$ 'th month. We use the same  $p_{\text{H}}$  parameter consistently for every pressure level, month, and for the ground-based meteorological data. The resulting vertical profile will be, in most cases, a combination of data taken at different days, but the parametrisation assures that imposing a stronger selection criterion (i.e. lowering  $p_{\text{H}}$ ) results in a lower column PWV, as expected. In order to average over the year-to-year variability of PWV, and approximate the climate for a given month, we split the IGRA records into yearly sub-samples, which we analyse separately. Then, for any given month and pressure level the mean RH is calculated for all years. The exact value of the  $p_{\text{H}}$  selection parameter, that would be compatible with cloudless skies, and would not concern only the driest conditions, is unknown, but can be constrained by independent PWV measurements, performed in clear sky conditions (see Sec. 2.6).

The downside of such parametrisation is that the probability distribution function (PDF) for the  $p_{\text{H}}$  selection parameter, by construction, is zero outside of  $[0, 1]$  range. This is because  $p_{\text{H}}$  is associated with the probability of obtaining a RH measurement smaller than the quantile function (Eq. 5) for a given pressure level, month and year. The final monthly-average profile is a multi-year mean, therefore even for the maximum value of  $p_{\text{H}} = 1$  – i.e. when no data is filtered out – the resulting average model will not be able to describe an individual day with PWV values above the mean. However, in the current approach we are focused on a parametrisation that is suitable for the average clear sky model, and will accept these limitations since we are not going to analyse the significance of deviations of individual measurements from the mean.

In order to account for the large diurnal variation of RH and to enable a meaningful comparison between different days, we select the RH data records acquired between hours 10 and 14 (UTC+1), where the temperatures should be least affected by the diurnal variation of the solar irradiance. Hence, the differences in RH between different days, better reflect the actual PWV content variations, and not temperature variations.

## 2.6 PWV measurements

We have been monitoring PWV, expressed in column millimetres of water ( $w$ ), in the clear sky conditions since June 2013. A compilation from the first data release is summarised in Table 1. The measurements were performed using a hand-held MICROTOPS II sun photometer at the Meteorological Observatory of the Department of Meteorology and Climatology of the Nicolaus Copernicus University in Toruń (hereafter DMC). In what follows, we will refer to our sun photometer PWV measurements as *TR-PWV-DR-1*.

The atmospheric column PWV is calculated along LOS

towards the Sun, based on photometric measurements of water absorption peak at 936 nm, and of the continuum at 1020 nm (without water absorption). The PWV resulting from Beer-Lambert-Bouguer's law is converted to the zenith column water abundance based on the Sun's zenith distance at the time and location of the measurement. The accuracy of the measurement is 0.1 mm. Using a reference MICROTOPS II sun photometer we verified that with the factory settings the systematical differences to measure PWV between different instruments is  $\Delta w \lesssim 0.1$  mm.

The data have been collected only in clear sky conditions, which allows us to quantify the PWV variations due to air masses carrying different amounts of water vapour, depending on seasons and winds. The data are typically taken every hour and every observation contains several measurements that are averaged. In stable clear sky conditions the differences between hourly samples are small (relative to our measurement precision) and we use a daily mean as a single data record. Then, the monthly average, standard deviation and extreme values are calculated from daily records (Table 1).

We also utilise the publicly available PWV data from AERONET<sup>7</sup> robotic stations, which automatically trace the Sun and measure the atmospheric water lines spectrum. We use the data from the Belsk station in Poland (near Warsaw), collected between (and including) years 2002 and 2014. Since the AERONET data are collected automatically and exclude only the periods of rain, the raw data may be contaminated by the presence of clouds and therefore should be more compatible with the average PWV abundances reconstructed from climatology data: i.e. without imposing any selection criteria. The AERONET data are essentially provided at three levels of post-processing. Level 1.0 is raw data (Fig. 5). Level 1.5 data are automatically screened for clouds based on number of simple criteria involving time and spectral stability of the measured optical depths (Smirnov et al. 2000), and level 2.0 data, which we use in our analysis, are further corrected manually for glitches and any other abnormalities that could elude automatic screening.

The difference between our measurements and the AERONET level 2.0 data (Fig. 5) is that the latter have clouds removed directly from the LOS towards the Sun, thus not guaranteeing a cloudless sky. Our sample however, in most cases was taken during cloudless days, at the penalty of fewer measurements.

## 3 SOLVING RADIATIVE TRANSFER THROUGH ATMOSPHERIC LAYERS

In this section we briefly review the principal equations of radiative transfer and outline the calculation scheme.

Based on a model of the vertical structure of the atmosphere we calculate the column PWV ( $w$ ), atmospheric brightness temperature ( $T_{\text{atm}}$ ), optical depth ( $\tau$ ) and the corresponding transmittance ( $t_{\text{atm}} = e^{-\tau}$ ) using the AM program (version 7.2) – a publicly-available radiative transfer solver, developed at the Harvard-Smithsonian Center for Astrophysics (Paine 2012).

<sup>7</sup> <http://aeronet.gsfc.nasa.gov>

Propagation of radiation through a medium is given by the radiative transfer equation

$$\frac{dI_\nu}{ds} = -\kappa_\nu I_\nu + \epsilon_\nu, \quad (6)$$

where  $I_\nu$  is the specific intensity and  $\kappa_\nu = -\frac{d\tau_\nu}{ds}$ , is the total opacity due to absorption and scattering,  $\tau_\nu$  is the optical depth, and  $\epsilon_\nu$  is the emissivity along the propagation path  $s$ . In the case of local thermodynamic equilibrium (LTE) the radiative transfer equation can be rewritten (Wilson et al. 2009) as:

$$-\frac{1}{\kappa_\nu} \frac{dI_\nu}{ds} = \frac{dI_\nu}{d\tau} = I_\nu - B_\nu(T), \quad (7)$$

where  $B_\nu(T)$  is the Planck radiance. The solution is given by:

$$I_\nu(s) = I_\nu(0)e^{-\tau_\nu(s)} + \int_0^{\tau(s)} B_\nu(T(\tau))e^{-\tau_\nu} d\tau. \quad (8)$$

For a thin atmospheric layer, inside which the temperature can be assumed constant, Eq. 8 can be integrated as

$$I_\nu(s) = I_\nu(0)e^{-\tau_\nu(s)} + B_\nu(T)(1 - e^{-\tau_\nu(s)}), \quad (9)$$

where the first term on the right hand side is the incident radiance that is exponentially attenuated along the propagation path. The second term amounts to the thermal emission of the layer corrected for the self-absorption, required to maintain the assumed LTE. The spectrum of the optical depth is medium dependent and can be derived from the quantum-mechanical properties of atoms and molecules present in the medium. The effects leading to a violation of the LTE, such as thermal conduction or convection are reasonably neglected.

The radiative transfer equation is solved for each absorbing (emitting) species and for each atmospheric layer. We use  $N_L = 300$  stacked layers, each characterised by its pressure ( $P$ ), temperature ( $T$ ), geometrical thickness, and chemical composition: a mixture of nitrogen, oxygen, ozone, and water vapour defined in terms of VMRs. The layers are homogeneously distributed in log-altitude space, which roughly corresponds to a homogeneous distribution in pressure space. We use the same definition of layers for all atmospheric species. The lowermost layer altitude,  $z = 133$  m, is chosen to coincide with the altitude of RT32. The uppermost layer altitude is assumed to be  $z_{\max} = 60$  km.

It is assumed that the incident (background) radiation has initially Planckian distribution ( $B_\nu(T)$ ) with  $T = T_{\text{CMB}} = 2.726$  (Fixsen 2009) – the thermodynamic temperature of the Cosmic Microwave Background radiation (CMB). Thus, our definition of  $T_{\text{atm}}$  includes the contribution of CMB.

Calculations are performed towards zenith or at directions located at the zenith distance  $z_d$ , and layers are assumed to have a flat geometry. The brightness temperature  $T_{\text{atm}}$  is obtained by solving

$$I_{\nu,\text{atm}} = B_\nu(T_{\text{atm}}) \quad (10)$$

where  $I_{\nu,\text{atm}}$  is the output radiance at the lowermost atmospheric layer. The brightness temperature spectrum is calculated within the frequency range  $\nu = [1, 60]$  GHz with 50 MHz resolution. Details of the physical processes taken into account are described in the AM program technical memo (Paine 2012).

## 4 RESULTS

### 4.1 Precipitable Water Vapour

A compilation of the *TR-PWV-DR-1* measurements (Sec. 2.6) is shown in Fig. 5, and the corresponding data are gathered in Table 1. In this figure solid (cyan) lines represent the PWV models calculated using the climatological data discussed in Sec. 2.1–2.4. The line width is increased with the increases of the  $p_{\text{H}}$  selection parameter (Sec. 2.5). For any given month, the reconstructed column PWV is assumed to occur at mid-month.

We constrain the value of the  $p_{\text{H}}$  parameter, which implies the PWV level that is expected to occur in clear sky conditions. We use a  $\chi^2$  minimisation, neglecting the cross-month covariance:

$$\chi^2 = \sum_{i=1}^{12} [\langle w \rangle_i - \mathcal{M}_i(p_{\text{H}})]^2 / \sigma_i^2, \quad (11)$$

where  $\langle w \rangle_i$  and  $\sigma_i^2$  are the  $i$ 'th month PWV mean and standard deviation respectively, and  $\mathcal{M}_i(p_{\text{H}})$  is the model PWV value interpolated at the locus of the  $i$ 'th month data point. When the monthly variance estimate is unknown (due to missing data), it is interpolated from the neighbouring months (with continuity across Dec/Jan).

Given the PWV data  $\mathcal{D}$ , and the reconstructed PWV model  $\mathcal{M}$ , parametrised by  $p_{\text{H}}$ , we define the posterior probability for  $p_{\text{H}}$  using the Bayes theorem:

$$\mathcal{P}(p_{\text{H}}|\mathcal{M}, \mathcal{D}) \propto \mathcal{L}(\mathcal{D}|\mathcal{M}, p_{\text{H}})\Pi(p_{\text{H}}|\mathcal{M}) \quad (12)$$

where  $\mathcal{L}(\mathcal{D}|\mathcal{M}, p_{\text{H}})$  is the likelihood of the data given the model and  $\Pi(p_{\text{H}}|\mathcal{M})$  is the prior imposed on the parameter probability distribution function (PDF). By design, the PDF for the  $p_{\text{H}}$  parameter is zero outside  $[0, 1]$  range (see Sec. 2.5). We assume the AERONET data as a prior and obtain the maximum posterior constraint on the  $p_{\text{H}}$  parameter and calculate the 68% confidence interval. The likelihood function is probed using the sun photometer data (Fig. 6). However, we also analyse each of the datasets alone. Constraints on the  $p_{\text{H}}$  parameter are gathered in Table 2. As indicated by the vertical lines in Fig. 6, *TR-PWV-DR-1* and the AERONET/Belsk datasets are compatible at the 68% CL, but the maximum-likelihood  $p_{\text{H}}$  parameter value is lower for the earlier data, which we attribute to the fact that the *TR-PWV-DR-1* sample was collected under excellent weather conditions, which guaranteed a cloudless sky, and therefore statistically favoured lower PWV abundances.

From Fig. 5 it is clear that the year-around distribution of AERONET/Belsk PWV follows very closely the shape of the reconstructed models with high  $p_{\text{H}}$  values (corresponding to weak data selection). The strength of the correlation is also reflected in the smallness of the best fit  $\chi^2/\text{DOF}$  value, although the dispersion of the individual PWV measurements (from which the monthly variance is calculated) is relatively large in both data samples. Clearly, AERONET/Belsk level 1.0 dataset corresponds to a greater  $p_{\text{H}}$  value than level 2.0 dataset, as expected.

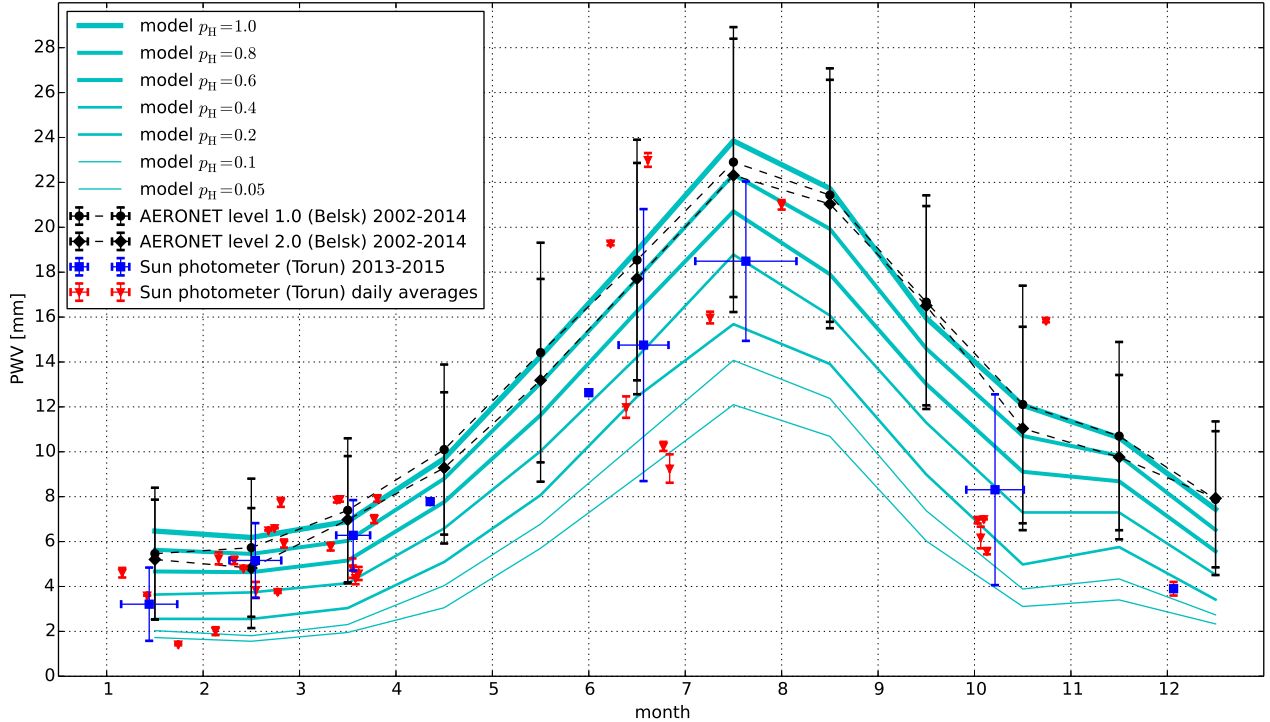


**Figure 5.** A compilation of PWV measurements. The monthly averages from our *TR-PWV-DR-1* sample are marked with blue squares while the daily averages are marked with red triangles. The error bars correspond to  $\pm 1\sigma$  deviation from the mean. The black diamonds (dots) are the AERONET data level 2.0 (1.0) from the Belsk station. The cyan lines represent our PWV models reconstructed from climatology data described in Sec. 2. The thickness of an individual solid line increases with  $p_H$ . The increases correspond to a progressively less aggressive selection of the climatology data by low RH values (Sec. 2.5).

#### 4.2 Average clear sky atmospheric brightness temperature and optical depth: case for Toruń, Poland

With the reconstructed vertical structure of the atmosphere (Sec. 2) we now determine the local  $T_{\text{atm}}$  and  $\tau$  using the radiative transfer solver described in Sec. 3.

In Fig. 7 we plot the best-fit local  $T_{\text{atm}}$  models up to the Q-band frequencies. The most prominent atmospheric feature is associated with the water line that is Doppler- and pressure-broadened about the resonance frequency  $\nu_0 \approx 22.235$  GHz. On the top of the broad band emission a very weak and sharp contribution is found due to a thermally-excited stimulated emission. This is seen as a tiny increase of  $\Delta T_{\text{atm}} \approx 0.15$  K exactly at the resonance frequency  $\nu_0$ , however effects of fluctuating PWV levels due to atmospheric turbulence (see Sect. 4.4) generate  $T_{\text{atm}}$  variations of the same order in the time scale of hours or less.

Clearly,  $T_{\text{atm}}$  and  $\tau$  are strongly season-dependent, as is the level of PWV. The high-frequency tail of  $T_{\text{atm}}$  in Fig. 7 is caused by the contribution from the oxygen  $O_2$  line that is insensitive to PWV content. The only way to mitigate this emission is to observe at higher altitudes, i.e. through a thinner atmosphere. In Fig. 7 the legend provides the value of column PWV in millimetres for each model. For comparison, the mean PWV level on the South Pole in the austral winter is about 0.26 mm (Bussmann et al. 2005) which is  $\sim 25$  times lower as compared to the mean PWV content in January in Legionowo (Poland) and  $\sim 12$  times lower than

the mean PWV content in clear sky conditions measured in Toruń (Table 1). However, since the WV brightness temperature spectrum depends on temperature, a comparison of radiative properties between the two sites based on the PWV levels difference is not straightforward.

The impact of ozone is seen only in spectral lines, which are weak in the Q-band, as compared to the effects caused by atmospheric instabilities. We re-calculate the spectra with the resolution of 5 kHz and observe that the lines amplitude is well below 1 K above the continuum at the resonance frequencies. However, the ozone contribution becomes more important at higher frequencies.

From Fig. 7 it is clear that lower PWV levels result in lower  $T_{\text{atm}}$  values. The stratospheric PWV levels, as traced by satellites, are roughly constant throughout the year. We observe that above 13 km the levels are very low, in the order of a few  $\mu$ -metres:  $w \sim 0.005$  mm in January and July, and therefore the stratospheric PWV impact on  $T_{\text{atm}}$  seems unimportant for the ground level sites.

We use the best fit model determined by the combined AERONET/Belsk and Toruń data samples (Table 2) to calculate the local  $T_{\text{atm}}$  and  $\tau$  for each month. The result is shown in Table 3. In that table the error bars correspond to the variation of the  $p_H$  selection parameter within the 68% CR.

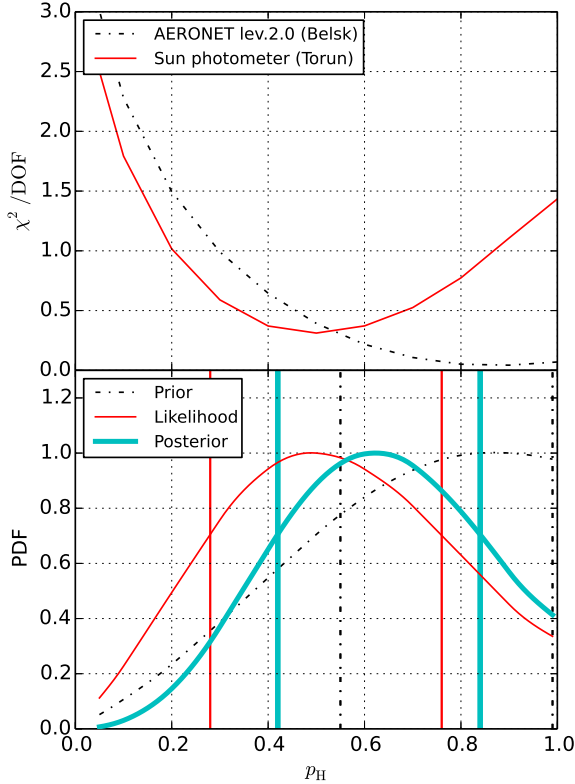


**Figure 6.** Constraints on  $p_H$  selection parameter (see Sec. 2.5). The vertical lines in the bottom panel encompass the 68% CR, as summarised in Table 2. The three PDFs are obtained from the AERONET/Belsk PWV data (black, dash-dotted), Toruń MICROTUPS measurements (red, solid thin), and the two datasets combined (solid thick).

### 4.3 Atmospheric approximations and zenith distance dependence

In common observational practice simplifying approximations are introduced at the cost of accuracy. These approximations rely on assumptions that the atmosphere: (i) is composed of a single homogeneous layer, (ii) has a flat geometry and (iii) is optically thin. In the following sections we briefly discuss these assumptions in the light of the reconstructed atmospheric model.

#### 4.3.1 Single-layer atmosphere

A single layer atmosphere has a single physical temperature  $T$  (Eq. 9) that is often assumed to be somewhere between 250 K and 290 K. However, given the reconstructed atmospheric model it is easy to derive this value.

From Eq. 8 the atmospheric emission of a multi-layer, flat atmosphere with a vertical temperature profile can be written as:

$$I_{\nu,\text{atm}} = B_{\nu}(T_{\text{CMB}})e^{-\tau(z_d)} + \sum_{i=1}^N B_{\nu}(T_i)(1 - e^{-\tau_i(z_d)}), \quad (13)$$

where  $T_i$  is the  $i$ 'th layer temperature,  $\tau_i$  is its optical depth,

**Table 1.** Compilation of column PWV measurements ( $TR$ -PWV-DR-1) performed in clear sky conditions using MICRO-TOPS II sun photometer (Sec. 2.6).

Location <sup>a</sup>	18° 34' 04.8'' E, 53° 01' 12.0'' N			
Period	2013/06/07 – 2015/04/13			
Duration <sup>b</sup>	~ 17 months			
Month	$\langle w \rangle^c$ [mm]	Min/Max <sup>d</sup> [mm]	# of days <sup>e</sup>	Cmt <sup>f</sup>
1	3.2 ± 1.6	1.4 / 4.6	3	
2	5.2 ± 1.7	2.0 / 7.7	10	
3	6.3 ± 1.6	4.4 / 7.9	8	
4	7.8 ± 0.1	7.8 / 7.8	1	SD
5	12.6 ± 0.1	12.6 / 12.6	1	SD
6	14.8 ± 6.1	9.3 / 23.0	5	
7	18.5 ± 3.5	16.0 / 21.0	2	
8			0	ND
9			0	ND
10	8.3 ± 4.2	5.6 / 15.8	5	
11			0	ND
12	3.9 ± 0.1	3.9 / 3.9	1	SD

<sup>a</sup>Geodetic coordinates of the observation site (DMC).

<sup>b</sup>Effective number of observed months. No-observation periods: Aug–Sep 2013 and Jul–Oct 2014.

<sup>c</sup>Monthly average and a standard deviation of PWV, both calculated using daily means.

<sup>d</sup>PWV data extremal values

<sup>e</sup>The total number of days observed in a given month.

<sup>f</sup>Comment: SD - single day mean and standard deviation, ND - no data

**Table 2.** 68% CL constraints on  $p_H$  selection parameter from the sun photometer data (Table 1), from the AERONET/Belsk data and from the two datasets combined.

	Sun Phot. (Toruń)	AERONET (Belsk, lev. 2.0)	Combined
$\min\left(\frac{\chi^2}{\text{DOF}}\right)$	~ 0.31	~ 0.04	NA
$p_H$	(0.28, 0.76)	(0.55, 1.00)	(0.42, 0.84)
MOD( $p_H$ )	0.49 <sup>+0.27</sup> <sub>-0.21</sub>	0.87 <sup>+0.12</sup> <sub>-0.32</sub>	0.62 <sup>+0.22</sup> <sub>-0.20</sub>
EX( $p_H$ )	0.53	0.65	0.62

and  $N$  is the total number of layers (Sec. 3).  $I_{\nu,\text{atm}}$  is the calculated atmospheric specific intensity, for which the brightness temperature is given by Eq. 10. and is tabulated along with  $\tau$  in Table 3. An obvious consequence of considering a multi-layer atmosphere is that it does not have a single physical temperature, because it is a combination of multiple components, each having a different temperature (Eq. 13). A multi-layer atmosphere however can be assigned a single-layer atmosphere equivalent temperature,  $T_{\text{SL}}$ , that yields:

$$I_{\nu,\text{atm}} = B_{\nu}(T_{\text{CMB}})e^{-\tau(z_d)} + B_{\nu}(T_{\text{SL}}(\nu))(1 - e^{-\tau(z_d)}). \quad (14)$$

Combining Eq. 13 and Eq. 14 gives

$$T_{\text{SL}}(\nu) = \frac{h\nu}{k_B \ln D}, \quad (15)$$

$$D = \frac{2h\nu^3}{c^2} \frac{1 - e^{-\tau(z_d)}}{I_{\nu,\text{atm}} - B_{\nu}(T_{\text{CMB}})e^{-\tau(z_d)}} + 1.$$

**Table 3.** 68% CL constraints on the clear sky, zenith, mean atmospheric brightness temperature ( $T_{\text{atm}}$ ) and optical depth ( $\tau$ ). The values for the selected frequencies and months are calculated according to the best fit PWV model selected by the combined AERONET/Belsk and Toruń data samples (Table 2). The asterisk (\*) marks the errors that are rounded up to appear non-zero at the provided accuracy.  $A$  and  $B$  are the linear-fit constants of the  $T_{\text{atm}} = A\langle w \rangle + B$  and  $t_{\text{atm}} = A\langle w \rangle + B$  scaling relations.  $A$  and  $B$  are written in scientific notation with the decimal exponent in parentheses.

	$\nu$ [GHz]	5	15	22	30	5	15	22	30
Month	$\langle w \rangle$	$T_{\text{atm}}$				$\tau$			
	[mm]	[K]	[K]	[K]	[K]	$\times 10^{-3}$	$\times 10^{-2}$	$\times 10^{-2}$	$\times 10^{-2}$
1	4.8 <sup>+1.1</sup> <sub>-1.0</sub>	5.10 <sup>+0.01</sup> <sub>-0.01</sub>	6.4 <sup>+0.1</sup> <sub>-0.1</sub>	14.6 <sup>+1.9</sup> <sub>-1.7</sub>	11.7 <sup>+0.5</sup> <sub>-0.5</sub>	9.50 <sup>+0.03</sup> <sub>-0.03</sub>	1.5 <sup>+0.1</sup> <sub>-0.1</sub>	4.7 <sup>+0.8</sup> <sub>-0.7</sub>	3.6 <sup>+0.2</sup> <sub>-0.2</sub>
2	4.7 <sup>+0.9</sup> <sub>-0.9</sub>	5.09 <sup>+0.01</sup> <sub>-0.01</sub>	6.3 <sup>+0.1</sup> <sub>-0.1</sub>	14.4 <sup>+1.5</sup> <sub>-1.5</sub>	11.7 <sup>+0.4</sup> <sub>-0.4</sub>	9.48 <sup>+0.03</sup> <sub>-0.04</sub>	1.4 <sup>+0.1*</sup> <sub>-0.1*</sub>	4.6 <sup>+0.6</sup> <sub>-0.6</sub>	3.6 <sup>+0.2</sup> <sub>-0.2</sub>
3	5.3 <sup>+1.0</sup> <sub>-1.0</sub>	5.09 <sup>+0.01</sup> <sub>-0.01</sub>	6.4 <sup>+0.1</sup> <sub>-0.1</sub>	15.5 <sup>+1.7</sup> <sub>-1.7</sub>	11.9 <sup>+0.5</sup> <sub>-0.5</sub>	9.39 <sup>+0.04</sup> <sub>-0.04</sub>	1.5 <sup>+0.1</sup> <sub>-0.1*</sub>	5.0 <sup>+0.7</sup> <sub>-0.7</sub>	3.6 <sup>+0.2</sup> <sub>-0.2</sub>
4	7.8 <sup>+1.2</sup> <sub>-1.2</sub>	5.12 <sup>+0.01</sup> <sub>-0.01</sub>	6.7 <sup>+0.2</sup> <sub>-0.2</sub>	19.9 <sup>+2.1</sup> <sub>-1.9</sub>	13.0 <sup>+0.6</sup> <sub>-0.6</sub>	9.34 <sup>+0.06</sup> <sub>-0.06</sub>	1.5 <sup>+0.1</sup> <sub>-0.1</sub>	6.6 <sup>+0.9</sup> <sub>-0.8</sub>	4.0 <sup>+0.2</sup> <sub>-0.2</sub>
5	11.8 <sup>+1.6</sup> <sub>-1.6</sub>	5.16 <sup>+0.01</sup> <sub>-0.02</sub>	7.3 <sup>+0.2</sup> <sub>-0.2</sub>	26.9 <sup>+2.8</sup> <sub>-3.0</sub>	14.9 <sup>+0.7</sup> <sub>-0.7</sub>	9.36 <sup>+0.06</sup> <sub>-0.07</sub>	1.7 <sup>+0.1</sup> <sub>-0.1</sub>	9.3 <sup>+1.2</sup> <sub>-1.1</sub>	4.6 <sup>+0.3</sup> <sub>-0.3</sub>
6	16.3 <sup>+1.7</sup> <sub>-1.9</sub>	5.20 <sup>+0.02</sup> <sub>-0.02</sub>	7.9 <sup>+0.2</sup> <sub>-0.2</sub>	34.7 <sup>+3.0</sup> <sub>-3.3</sub>	17.0 <sup>+0.8</sup> <sub>-0.9</sub>	9.40 <sup>+0.08</sup> <sub>-0.07</sub>	1.9 <sup>+0.1</sup> <sub>-0.1</sub>	12.3 <sup>+1.3</sup> <sub>-1.4</sub>	5.4 <sup>+0.3</sup> <sub>-0.3</sub>
7	20.9 <sup>+1.9</sup> <sub>-1.9</sub>	5.25 <sup>+0.02</sup> <sub>-0.02</sub>	8.5 <sup>+0.2</sup> <sub>-0.2</sub>	42.8 <sup>+3.2</sup> <sub>-3.2</sub>	19.2 <sup>+0.9</sup> <sub>-0.8</sub>	9.47 <sup>+0.08</sup> <sub>-0.07</sub>	2.1 <sup>+0.1</sup> <sub>-0.1</sub>	15.5 <sup>+1.4</sup> <sub>-1.4</sub>	6.1 <sup>+0.3</sup> <sub>-0.3</sub>
8	18.1 <sup>+2.4</sup> <sub>-1.8</sub>	5.23 <sup>+0.02</sup> <sub>-0.02</sub>	8.1 <sup>+0.3</sup> <sub>-0.2</sub>	38.0 <sup>+4.0</sup> <sub>-3.2</sub>	17.9 <sup>+1.1</sup> <sub>-0.8</sub>	9.43 <sup>+0.08</sup> <sub>-0.07</sub>	2.0 <sup>+0.1</sup> <sub>-0.1</sub>	13.6 <sup>+1.7</sup> <sub>-1.4</sub>	5.7 <sup>+0.4</sup> <sub>-0.3</sub>
9	13.0 <sup>+1.9</sup> <sub>-1.7</sub>	5.18 <sup>+0.02</sup> <sub>-0.02</sub>	7.5 <sup>+0.2</sup> <sub>-0.2</sub>	29.0 <sup>+3.3</sup> <sub>-2.9</sub>	15.5 <sup>+0.8</sup> <sub>-0.8</sub>	9.39 <sup>+0.07</sup> <sub>-0.07</sub>	1.8 <sup>+0.1</sup> <sub>-0.1</sub>	10.1 <sup>+1.4</sup> <sub>-1.2</sub>	4.8 <sup>+0.3</sup> <sub>-0.3</sub>
10	9.3 <sup>+1.8</sup> <sub>-1.7</sub>	5.15 <sup>+0.01</sup> <sub>-0.02</sub>	7.0 <sup>+0.2</sup> <sub>-0.2</sub>	22.6 <sup>+3.1</sup> <sub>-3.0</sub>	13.8 <sup>+0.8</sup> <sub>-0.8</sub>	9.36 <sup>+0.07</sup> <sub>-0.07</sub>	1.6 <sup>+0.1</sup> <sub>-0.1</sub>	7.7 <sup>+1.3</sup> <sub>-1.2</sub>	4.2 <sup>+0.3</sup> <sub>-0.3</sub>
11	8.7 <sup>+1.3</sup> <sub>-1.4</sub>	5.13 <sup>+0.01</sup> <sub>-0.01</sub>	6.9 <sup>+0.2</sup> <sub>-0.2</sub>	21.3 <sup>+2.2</sup> <sub>-2.3</sub>	13.5 <sup>+0.8</sup> <sub>-0.6</sub>	9.40 <sup>+0.06</sup> <sub>-0.06</sub>	1.6 <sup>+0.1</sup> <sub>-0.1</sub>	7.2 <sup>+0.9</sup> <sub>-1.0</sub>	4.2 <sup>+0.2</sup> <sub>-0.2</sub>
12	5.7 <sup>+1.2</sup> <sub>-1.0</sub>	5.11 <sup>+0.01</sup> <sub>-0.01</sub>	6.5 <sup>+0.1</sup> <sub>-0.1</sub>	16.2 <sup>+2.0</sup> <sub>-1.8</sub>	12.2 <sup>+0.5</sup> <sub>-0.5</sub>	9.48 <sup>+0.04</sup> <sub>-0.05</sub>	1.5 <sup>+0.1</sup> <sub>-0.1</sub>	5.3 <sup>+0.8</sup> <sub>-0.7</sub>	3.7 <sup>+0.2</sup> <sub>-0.2</sub>
Mean	10.5	5.15	7.1	24.7	14.4	9.42	1.7	8.5	4.5
St.Dev.	5.5	0.05	0.7	9.7	2.6	0.05	0.2	3.7	0.9
$A$		9.812(-03)	1.339(-01)	1.753(+00)	4.621(-01)	-4.544(-06)	4.046(-04)	6.676(-03)	1.567(-03)
$B$		5.047(+00)	5.713(+00)	6.185(+00)	9.492(+00)	9.475(-03)	1.249(-02)	1.458(-02)	2.811(-02)

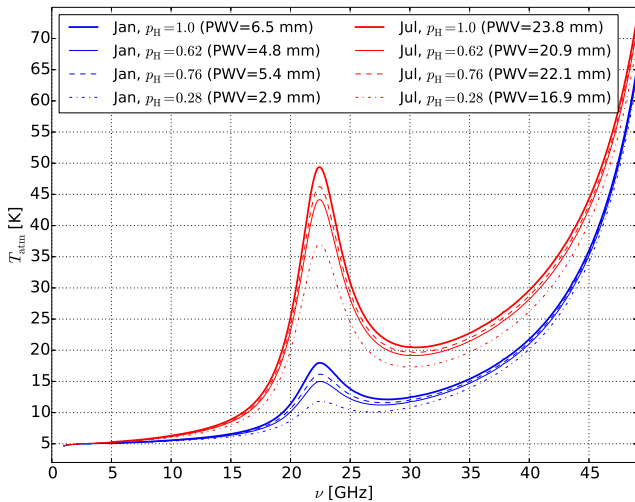


**Figure 7.** Average atmospheric brightness temperature as a function of frequency. The upper (red) lines correspond to July and lower (blue) lines correspond to January in Toruń. Within each group the thick solid line traces  $T_{\text{atm}}$  corresponding to the model obtained without imposing any selection criteria on the climatology data ( $p_{\text{H}} = 1.0$ ). Thin solid lines are calculated according to the best fit models found using the combined (Toruń + AERONET/Belsk) PWV data samples. The best fit  $p_{\text{H}}$  selection parameter values are given in the plot legend and in Table 2. The dashed and dash-dotted lines enclose the 68% confidence region, derived using the Toruń PWV data sample alone ( $TR$ -PWV- $DR$ -1). All curves are calculated for the zenith distance  $z_d = 0^\circ$  at the RT32 altitude ( $z = 0.133$  km).

For a single layer atmosphere  $N = 1$  and  $T_{\text{SL}} = T_1$ , and it is frequency independent. In general, however,  $T_{\text{SL}}$  depends on frequency because in different layers the temperature  $T_i$  (Eq. 13) is weighted by coefficients  $\sim (1 - e^{-\tau_i})$  that depend on frequency differently than  $(1 - e^{-\tau})$  (Eq. 9), and hence the frequency dependence does not cancel.  $T_{\text{SL}}$  is obviously season dependent too, and it can be readily derived from Eq. 15 using Eq. 10,  $T_{\text{atm}}$  and  $\tau$  estimates from Table 3. However, in the optically thin limit,  $T_{\text{SL}}$  is a sensitive function of  $T_{\text{atm}}$  and  $\tau$ .  $T_{\text{SL}}$  is also a weak function of zenith distance. At zenith, in the optically thin limit, it is a combination of all atmospheric layers, but near the horizon the lowermost atmospheric layers begin to dominate all other contributions. Within the flat-atmosphere model,  $T_{\text{SL}}$  will reach the ground-level atmospheric temperature at the horizon, but it will still vary from one season to another. In the optically thick limit,  $T_{\text{SL}} = T_{\text{atm}}$  and it also loses its frequency dependence because in this limit, the geometry is reduced to a single layer case.

In Fig. 8 we plot the calculated  $T_{\text{SL}}$  temperatures. Individual curves result from the best fit atmospheric models calculated for the selected months. The spectra were calculated using Eq. 15, but due to the strong sensitivity of  $T_{\text{SL}}$  to  $\tau$  and  $T_{\text{atm}}$  the values cannot be constrained to a precision better than  $O(10)$  K from the current data.<sup>8</sup> The dents coincide with the resonance frequencies of water and ozone lines.

For any given frequency the single-layer atmosphere equivalent temperature ( $T_{\text{SL}}$ ) should be most affected by

<sup>8</sup> For example, a variation of  $\tau$  by  $10^{-3}$  at 30 GHz in July implies a  $\sim 4$  K change in  $T_{\text{SL}}$  (Table 3).

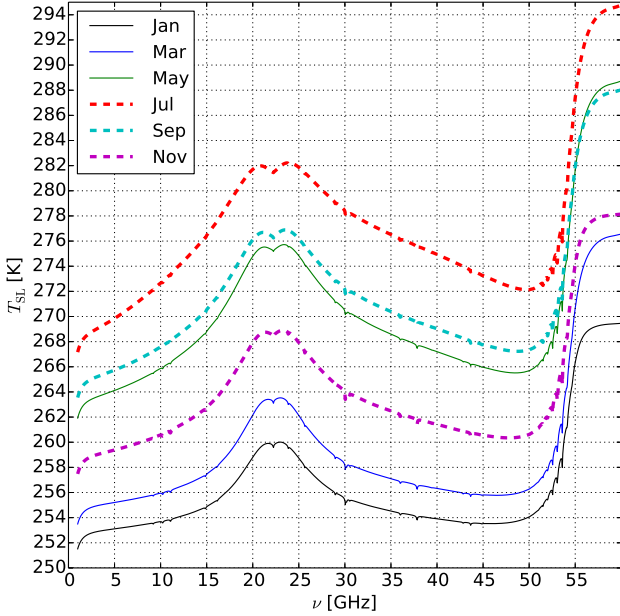


**Figure 8.** Single-layer atmosphere equivalent temperature resulting from the best fit model obtained from the combined PWV data samples (Table 2). The thin (solid) lines from the bottom to the top correspond to January, March and May, and the thick (dashed) lines from the top to the bottom are calculated for July, September and November.

the physical temperatures of layers that are most responsible for absorption of radiation at that frequency. About 50% of total WV contribution to  $T_{\text{atm}}$  takes place above altitudes 1-2 km (where the temperature is at least 5-10 K below the ground temperatures). At these altitudes there is also the biggest concentration of WV. Similarly, the typical height scale for  $\sim 50\%$  of oxygen absorption is about  $\sim 5$  km with typical temperatures  $\sim 30$  K lower than ground temperatures.<sup>9</sup> Since at 30 GHz the contributions to  $T_{\text{atm}}$  from oxygen and WV are similar, the expected single-layer atmosphere equivalent temperature should be about  $\sim 20$  K lower than the ground temperature. The result of a numerical calculation at 30 GHz is shown in Fig. 9. Clearly, for the location of TCfA a reasonable estimate of  $T_{\text{SL}}$ , at 30 GHz, can be found from the ground level temperatures, offset by  $\sim 15.7$  K. The offset for other frequencies can be inferred from Fig. 8. Given the sensitivity of  $T_{\text{SL}}$  (Eq. 15) to  $\tau$ , the offset ground-level atmospheric temperature may provide a better constraint than measurements of  $\tau$  and  $T_{\text{atm}}$ .

As mentioned earlier,  $T_{\text{SL}}$  also depends on zenith distance, but we find that the dependence is rather weak. Up to  $z_d = 75^\circ$ ,  $T_{\text{SL}}(z_d)$  is roughly constant and fixed at its zenith value, with accuracy better than  $\{0.2, 0.3, 1.5, 0.8\}$  K at frequencies  $\nu = \{5, 15, 22, 30\}$  GHz in July. Deviations from the zenith values are even smaller in January.

<sup>9</sup> Rough estimates found using the best-fit model in July.

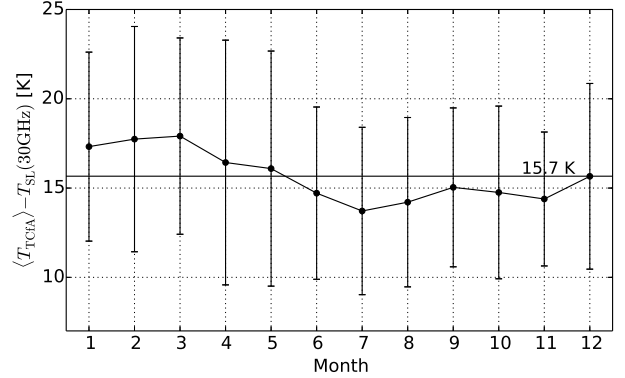


**Figure 9.** Relationship between the single-layer atmosphere equivalent temperature,  $T_{\text{SL}}$ , at 30 GHz, at the zenith (see Eq. 15) and the ground-level month-median atmospheric temperature at TCfA. The difference between the two is consistent, within  $\pm 1\sigma$  error bars, with a constant offset of about 15.7 K. The error bars represent the monthly ground-level temperature dispersion at TCfA. The median and standard deviation of the ground-level atmospheric temperatures are calculated using the meteorological data introduced in Sec. 2.4. The error bars are large as they include diurnal temperature variations.

#### 4.3.2 Planar atmosphere

Radio telescopes with an Az-El mount cannot efficiently observe sources towards the zenith, thus from practical reasons the dependence of  $T_{\text{atm}}$  on zenith distance ( $z_d$ ) is important. Based on the Bemporad’s air-mass-zenith-distance fitting formula (see Schoenberg (1929) or Wilson et al. (2009)), it can be seen that the assumption of flatness of the atmosphere – i.e. the atmosphere being composed of flat layers stacked one over another – is consistent with  $\sec(z_d)$  scaling to within 0.25% (3%) up to  $z_d < 60^\circ$  ( $80^\circ$ ). Within this approximation (which we use) the atmospheric optical depth is given by

$$\tau(z_d) = \tau(0) \sec(z_d), \quad (16)$$

where  $\tau(0) \equiv \tau(z_d = 0^\circ)$ . We assess the accuracy of this approximation by means of radiative transfer through atmospheric layers, whose thicknesses are increased to match ray path lengths travelling through spherical layers at given zenith angle. As before, we use the same setup of  $N = 300$ , layers distributed as discussed in Sec. 3, but in this case each layer is assumed to be located between geocentric radii  $R_i$  and  $R_j$  and hence its thickness  $h_{ij} = R_j - R_i$  at the zenith angle  $z_d$  (measured from the surface of the Earth), is given by:

$$h_{ij}(z_d) = (R_i^2 + R_j^2 - 2(R_\oplus^2 + C_i C_j) \sin^2(z_d))^{1/2} \quad (17)$$

$$C_i = \sqrt{R_i^2 \csc^2(z_d) - R_\oplus^2}$$

$$C_j = \sqrt{R_j^2 \csc^2(z_d) - R_\oplus^2},$$

where we assumed spherical Earth.

For each month, we use the best-fit atmospheric profile and calculate  $\tau(z_d)$  relations for a range of zenith distances, at the frequencies  $\nu[\text{GHz}] = \{5, 15, 22, 30\}$ . Then, we

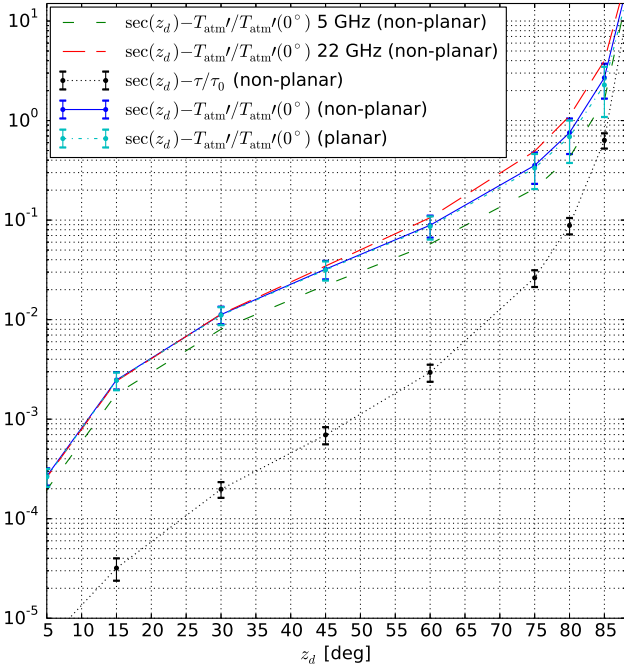


**Figure 10.** Mean zenith distance dependence of  $\tau/\tau(0)$  (black,dotted), and  $T'_{\text{atm}}(z_d)/T'_{\text{atm}}(0)$  (blue,solid and cyan,dash-dotted) for the best-fit local atmospheric model. Error bars represent  $\pm 1\sigma$  deviation from the mean due to frequency and monthly dependence. The short (long) dashed lines trace the season averaged dependence at 5 GHz (22 GHz).

normalise  $\tau(z_d)$  at the zenith and average between different frequencies and seasons. The differences between individual months (January and July) and frequencies vary between 40 and 53 at the horizon, and between 30 and 35 at  $z_d = 89^\circ$ , and between 10.6 and 11 at  $z_d = 85^\circ$ .

The following fourth order in  $\sec(z_d)$  fitting function provides a good fit to the reconstructed average relation, with the maximal deviation below 0.3% at  $z_d = 89^\circ$ :

$$\left\langle \frac{\tau(z_d)}{\tau(0)} \right\rangle = 1.001 \sec(z_d) - 3.739 \cdot 10^{-4} \sec^2(z_d) - 4.666 \cdot 10^{-4} \sec^3(z_d) + 6.0366 \cdot 10^{-6} \sec^4(z_d) \quad (18)$$

We do not use  $z_d = 90^\circ$  data point to avoid infinite values, but since the effects of refraction are not taken into account, the usability of the formula is effectively reduced down to  $z_d \lesssim 85^\circ$ , where the dispersion due to a seasonal and frequency dependence becomes similar to uncertainties due to neglected refraction.

According to the fitting formula, the assumption of the flat atmosphere (Eq. 16) is accurate to within 0.16 (1.6)% at  $z_d = 60^\circ$  ( $80^\circ$ ), where  $\langle \tau(z_d)/\tau(0) \rangle = 1.997 \pm 0.001$  ( $5.670 \pm 0.025$ ) and where the error bars represent the  $1\sigma$  dispersion due to season and frequency dependence.

To address the problem described at the beginning of this section, we calculate the average  $T'_{\text{atm}}(z_d)/T'_{\text{atm}}(0)$  relations for the planar and non-planar atmospheres (Fig. 10). This is useful because radio telescopes are directly sensi-

tive to increases of antenna temperature. The relations are derived according to the best fit atmospheric model (last column of Table 2). The  $\tau/\tau(0)$  relation for the planar case is given by  $\sec(z_d)$  and is not plotted, whereas the average  $\tau/\tau(0)$  for the non-planar case is given by Eq. 18 (black/dotted line in Fig. 10). The zenith distance dependence of  $T'_{\text{atm}}(z_d)/T'_{\text{atm}}(0)$  is given by the following fitting formula, which approximates the month and frequency averaged relation below  $z_d = 89^\circ$  (dash-dotted/cyan line in Fig. 10):

$$\left\langle \frac{T'_{\text{atm}}(z_d)}{T'_{\text{atm}}(0)} \right\rangle = 1.022 \sec(z_d) - 3.203 \cdot 10^{-2} \sec^2(z_d) + 9.625 \cdot 10^{-4} \sec^3(z_d) - 1.059 \cdot 10^{-5} \sec^4(z_d), \quad (19)$$

where  $T'_{\text{atm}}$  is atmospheric brightness temperature calculated for the case when the CMB is not present as a source term in the radiative transfer equation, and  $T'_{\text{atm}}(0) \equiv T'_{\text{atm}}(z_d = 0^\circ)$ .

Clearly, the difference of the mean  $T'_{\text{atm}}(z_d)/T'_{\text{atm}}(0)$  from  $\sec(z_d)$  scaling is  $\sim 0.1$  (0.4) or alternatively:  $(\sec(z_d) - T'_{\text{atm}}/T'_{\text{atm}}(0))/\sec(z_d) \approx 4\%$  (9%) at  $z_d = 60^\circ$  ( $75^\circ$ ), where the averaging is done over twelve months and the four considered frequencies (Fig. 10). Looking into individual frequencies, the month averaged  $\sec(z_d) - T'_{\text{atm}}/T'_{\text{atm}}(0) \approx \{0.06, 0.09, 0.11, 0.10\}$  for  $z_d = 60^\circ$  at  $\nu = \{5, 15, 22, 30\}$  GHz. The effects due to planarity are more than order of magnitude smaller. The difference between the averaged  $\tau/\tau(0)$  and  $T'_{\text{atm}}/T'_{\text{atm}}(0)$  scalings increases as the optical depth escapes beyond the optically thin limit. This is discussed in the next section.

#### 4.3.3 Optically thin atmosphere

Within the RJ approximation  $B_\nu(T) = 2\nu^2 k_B T/c^2$ , and Eq. 13 becomes:

$$T_{\text{atm}}(z_d) = T_{\text{CMB}} e^{-\tau(z_d)} + \sum_{i=1}^N T_i (1 - e^{-\tau_i(z_d)}). \quad (20)$$

The approximation of optically thin atmosphere is often exploited by utilising the first order expansion in  $\tau$

$$T_{\text{atm}}^{(1)}(z_d) = T_{\text{CMB}}(1 - \tau(z_d)) + T_{\text{SL}}\tau(z_d), \quad (21)$$

where, as before, we utilised the single layer equivalent temperature at the zenith (see below). We checked that in order to visualise the shortcomings of using the optically thin atmosphere approximation the differences due to introducing the RJ approximation are unimportant.

Depending on what is being measured,  $T_{\text{CMB}}$  contribution is sometimes treated independently from  $T_{\text{atm}}$ , as if the CMB was not processed by the altitude dependent absorption. Below, we quantify this approximation, but in general, since the CMB propagates through an absorbing and emitting medium, the two contributions (one from the atmosphere and the other from the CMB) cannot be treated separately. For this reason, our constraints on  $T_{\text{atm}}$  include the CMB as a source term in Eq. 7. Neglecting the CMB as a source term, Eq. 21 for the case of flat atmosphere (Eq. 16) becomes:

$$T_{\text{atm}}^{(1)}(z_d) = T_{\text{SL}}\tau(0) \sec(z_d), \quad (22)$$

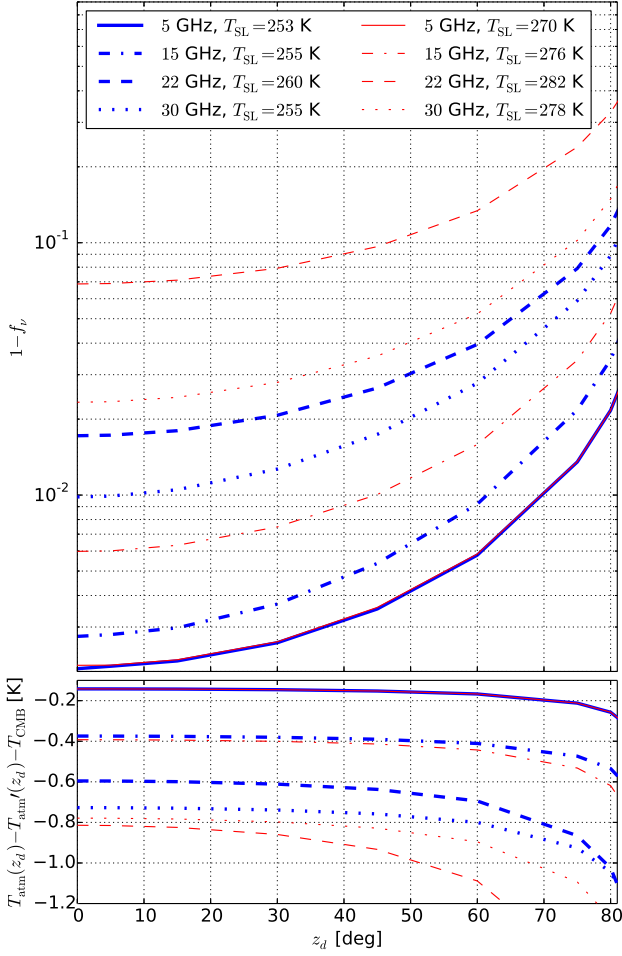


**Figure 11.** (Top panel) Accuracy of the atmospheric brightness temperature linear order expansion (Eq. 24) in January (blue/thick) and July (red/thin). The best-fit model ( $p_H = 0.62$ ) from the combined PWV data samples (Table 2) is used. For each frequency the zenith  $T_{SL}$  values are provided in the plot legend. (Bottom panel) Accuracy of  $T_{\text{atm}} \approx T_{\text{atm}}' + T_{\text{CMB}}$  approximation expressed as a difference between the actual  $T_{\text{atm}}$  and the sum of constituents considered separately:  $T_{\text{CMB}}$  and atmospheric brightness temperature derived without the CMB as a source term ( $T_{\text{atm}}'$ ).

and what follows is that for a single layer atmosphere

$$T_{\text{atm}}'(60^\circ) = 2T_{\text{atm}}'(0^\circ), \quad (23)$$

where  $T_{\text{atm}}'(z_d)$  is the atmospheric brightness temperature for  $T_{\text{CMB}} = 0$  K. This approximation is often used in tipping scan measurements.

Increasing the air mass, by looking at greater  $z_d$  angles, the linear-order approximation in Eq. 22 must fail at high values of  $\tau$  as  $T_{\text{atm}}$  (or  $T_{\text{atm}}'$ ) cannot reach infinity. The ratio of Eq. 20 and Eq. 21:

$$f_\nu(T_{\text{CMB}}, T_{\text{SL}}, \tau_0, z_d) = T_{\text{atm}}/T_{\text{atm}}^{(1)} \quad (24)$$

gives a factor by which  $T_{\text{atm}}$  is underestimated by using the linear-order single-layer approximation. Notice that Eq. 21, and consequently Eq. 22, introduce yet another, commonly used approximation, that  $T_{\text{SL}}$  does not depend on  $z_d$ , but instead is fixed at its zenith value. As discussed in Sec. 4.3.1,

this is quite a reasonable approximation for a range of  $z_d$ s.  $T_{\text{atm}}$  in Eq. 24 is calculated numerically within the flat atmosphere approximation, and  $T_{\text{atm}}^{(1)}$  is calculated according to Eq. 21 with  $\tau(z_d)$  derived numerically and with  $T_{\text{SL}}$  calculated from Eq. 15.

The factor  $f_\nu$  depends on  $\tau$ , frequency, and vertical temperature profile of the atmosphere. Assuming a flat and single-layer atmosphere without the CMB, it is easy to see that the factor becomes independent of atmospheric temperature and at  $z_d = 60^\circ$  amounts to  $f(T_{\text{CMB}} = 0 \text{ K}, \tau_0) = (1 - e^{-\tau_0 \sec(z_d)})/(\tau_0 \sec(z_d)) \approx 0.965(0.94)$  at 30 GHz for the best-fit value of  $\tau_0 = 0.036(0.061)$  in January (July) (Table 3).

In the bottom panel of Fig. 11 errors of considering  $T_{\text{CMB}}$  independently from  $T_{\text{atm}}$  are quantified. These are the lowest at low frequencies, small optical depths and small zenith angles (see plot description for details).

#### 4.3.4 Relation to observations

The approximations discussed in the previous sections may affect the radio source flux density observations at the levels of few to several per-cent.

In particular, estimates of the atmospheric absorption corrections may be biased depending on the assumed approximations. Flux-density absorption corrections within the flat and optically thin atmosphere model are given by:

$$S_t = S_m e^{\tau_0 \sec(z_d)} \approx S_m (1 + \tau_0 \sec(z_d)) \quad (25)$$

where  $S_t$  is the true flux density and  $S_m$  is the measured flux density. These corrections require an estimate of  $\tau = \tau(\nu, z_d, m)$ , which is a function of frequency ( $\nu$ ), zenith distance ( $z_d$ ), and month ( $m$ ).

With a single-dish radiometers  $\tau$  is typically estimated by measuring the system temperature components at the zenith and at  $z_d = 60^\circ$  with an implicit assumption of the validity of Eq. 23. In the simplest case, when detector linearity is assumed and the spillover, side-lobe and ground pick-up contributions are neglected, in the RJ approximation, the measurement can be defined by the following system of linear equations:

$$\begin{aligned} c_f V(0^\circ) &= T_{\text{atm}}'(0^\circ) + T_{\text{rx}} + T_{\text{CMB}} + \Delta T_\nu(0^\circ) \\ c_f V(60^\circ) &= A_m(60^\circ) T_{\text{atm}}'(0^\circ) + T_{\text{rx}} + T_{\text{CMB}} + \Delta T_\nu(60^\circ) \\ c_f V_{\text{abs}} &= T_{\text{abs}} + T_{\text{rx}}, \end{aligned} \quad (26)$$

where  $T_{\text{rx}}$  is the receiver noise temperature,  $T_{\text{abs}}$  is the absorber temperature and  $c_f$  is a conversion factor from the voltage, measured at the square-law detector, to the units of antenna temperature, and  $V(z_d)$  is the measured voltage at  $z_d$ .  $\Delta T_\nu$  is a correction factor weakly dependent on the zenith distance (Fig. 11 bottom panel). Usually, at  $z_d = 60^\circ$  the  $A_m = 2$  (and  $\Delta T_\nu = 0$ ) is assumed, in accordance with the flat atmosphere expectation.

Substituting thus derived value of  $T_{\text{atm}}'$  into Eq. 22 with an assumed value of  $T_{\text{SL}}$  gives an estimate of  $\tau$ . This is a possible source of systematical effects. First, as discussed in Sec. 4.3.1,  $T_{\text{SL}}$  follows ground level temperatures and fixing its value will lead to season dependent systematical effects. Secondly, Fig. 11 indicates that using an approximation given by Eq. 22 leads to a slight, but systematical

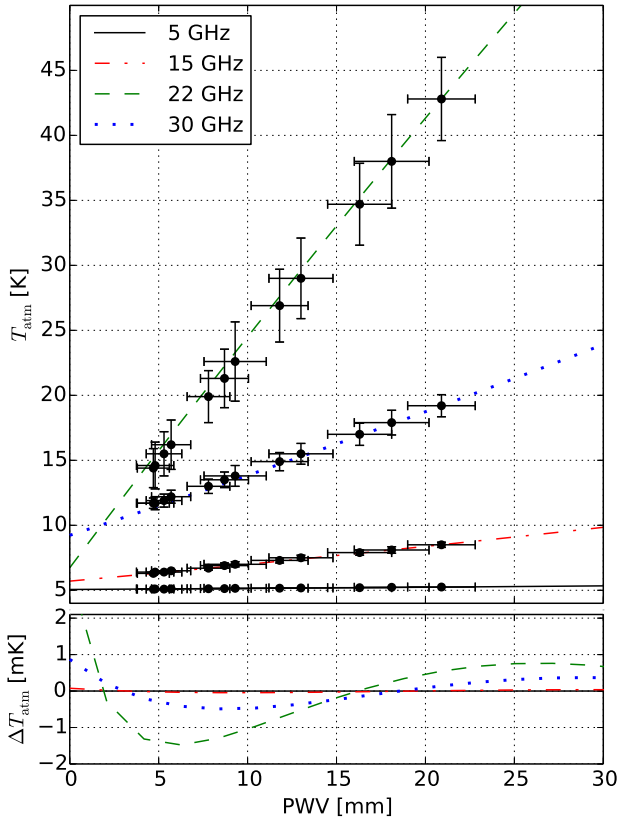


**Figure 12.** (*top panel*)  $T_{\text{atm}}$ -PWV scaling relations given by Eq. 27 and Table 4 (lines). The four sets of points over each of the lines represent the best-fit model brightness temperatures from Table 3. (*bottom panel*) Residues between the calculated scaling relations described in Sec. 4.4, and their respective fitting functions.

underestimation of  $\tau$  and  $S_t$ . In practice, absorption corrections are applied to both, the target source at  $z_d^{\text{src}}$  and the chosen flux calibrator at the zenith distance  $z_d^{\text{cal}}$ , hence the effects of the approximation in Eq. 22 on the relative flux density will cancel, as long as the calibrator and the target source happen to be observed at the same  $z_d$ . This is however almost never the case, and so the effects of the approximation will propagate onto the flux density estimates through factors  $\sim (1 + \tau_0 \sec(z_d^{\text{src}}))/(1 + \tau_0 \sec(z_d^{\text{cal}}))$ . Since the calibrator and target sources are observed at different elevations, this effectively leads to an increased variance of flux density estimates for individual sources, disparities between sources of the same intrinsic flux density, and possibly to systematical effects depending on source declination with respect to the calibrator.

#### 4.4 $T_{\text{atm}}/\tau$ -PWV scaling relation

In clear sky conditions and for a given vertical profile of PWV, there is a 1:1 relation between the measured PWV and  $T_{\text{atm}}$ . In this section we derive  $T_{\text{atm}}$ -PWV and  $\tau$ -PWV scaling relations for January and July, using the best fit model vertical profile estimates from the combined data samples (Table 2). In each profile the PWV content is scaled

at all altitudes by constant factors, and the corresponding  $T_{\text{atm}}$  and  $\tau$  are recorded. We calculate the scaling relations at frequencies 5,15,22 and 30 GHz and find that the following third order polynomial provides a good fit with negligible residues:

$$X = \sum_{i=0}^3 x_i \left( \frac{w}{1 \text{ mm}} \right)^i \quad (27)$$

where  $X = \{T_{\text{atm}}, \tau\}$  and  $x_i = \{a_i, b_i\}$ . The  $a_i$  and  $b_i$  coefficients are summarised in Table 4. Terms beyond the linear order describe the subtle effects of pressure line broadening and self-induced water vapour continuum absorption, both non-linearly dependent on  $\text{H}_2\text{O}$  VMR (Paine 2015). For  $\tau$  the scaling is quadratic and so we use the second order polynomial. In Fig. 12 we visualise  $T_{\text{atm}}$  scaling relations and the residual errors between these relations and their fitting formulas (Eq. 27).

The fitting formulas defined in Eq. 27 were derived using the best-fit models for January and July by scaling the WV content, hence the  $T_{\text{atm}}$  (or  $\tau$ ) predicted by these formulas will not exactly match the best-fit model values from Table 3. This is because the vertical structure of the atmosphere is month dependent. In order to visualise the amplitude of these differences, for each frequency, we over-plot the twelve  $T_{\text{atm}}$  values from Table 3 atop the fitting relation obtained for July (Fig. 12).  $T_{\text{atm}}$  from different months are consistent within  $1\sigma$  error bars quoted in Table 3, but a better consistency is reached at high PWV levels, typical for summer months, as expected. The year-average PWV- $T_{\text{atm}}$  scalings, which result from fitting the data points from Fig. 12, are given by  $A$  and  $B$  coefficients in Table 3.

$T_{\text{atm}}$ -PWV scaling relation can be used to estimate  $T_{\text{atm}}$  instabilities due to time varying column PWV. The amplitude of temporal fluctuations of the column PWV, under the frozen turbulence hypothesis, should constrain the spatial power spectrum of water vapour distribution at the scales  $L$ , roughly corresponding to  $v_w \Delta t$ , where  $\Delta t$  is the time interval between subsequent PWV measurements, and  $v_w$  is the wind speed at relevant altitudes. Alternatively, on the same assumptions, two instantaneous measurements of PWV, performed at two locations separated by distance  $L$ , probe the turbulent spectrum of PWV at the scales roughly corresponding to the spatial separation of the observation sites. While the spectrum of the atmospheric PWV fluctuations is beyond the scope of this paper, we discuss a rough estimate of the amplitude of the  $T_{\text{atm}}$  variations in clear sky conditions, based on the sun photometer measurements of the column PWV.

Since the  $T_{\text{atm}}$ -PWV scaling relation is dominated by the linear terms ( $a_0$  and  $a_1$ ) the  $a_1$  term can be thought of as an approximation of the derivative  $\frac{dT_{\text{atm}}}{dw}$  which quantifies  $T_{\text{atm}}$  response to variations in PWV ( $w$ ). Table 4 shows that PWV variation of  $\sim 0.2$  mm ( $\sim 0.3$  mm) would cause  $T_{\text{atm}}$  variation of the order  $\Delta T_{\text{atm}} \approx 0.09$  (0.14) K at 30 GHz in January (July). These are the amplitudes of the PWV variations in clear sky conditions we actually observe at  $\sim 1$ -hour time scales.<sup>11</sup> Clearly, low column PWV values also result in

<sup>10</sup> According to our notation  $T_{\text{atm}}$  includes the CMB as a source term (Sec. 3).

<sup>11</sup> The amplitude of the PWV variations quoted are examples

**Table 4.**  $T_{\text{atm}}$ -PWV and  $\tau$ -PWV fitting formula coefficients (Eq. 27). The numbers are written in scientific notation with the decimal exponent in parentheses. The 'error' column contains standard deviations of the difference between the derived scaling and the corresponding fitting formula.

$\nu$ [GHz]	January							
	$a_0$ [K]	$a_1$ [K/mm]	$a_2$ [K/mm <sup>2</sup> ]	$a_3$ [K/mm <sup>3</sup> ]	error [mK]	$b_0$	$b_1$ [mm <sup>-1</sup> ]	$b_2$ [mm <sup>-2</sup> ]
5	5.055(+00)	8.104(-03)	7.997(-05)	-2.841(-09)	2.441(-06)	9.350(-03)	3.108(-05)	3.047(-07)
15	5.738(+00)	1.282(-01)	6.849(-04)	-3.392(-07)	2.551(-04)	1.209(-02)	4.921(-04)	2.741(-06)
22	6.833(+00)	1.644(+00)	-3.827(-03)	8.033(-06)	1.434(-01)	1.650(-02)	6.391(-03)	5.896(-06)
30	9.477(+00)	4.603(-01)	2.396(-03)	-4.450(-06)	6.191(-03)	2.729(-02)	1.792(-03)	1.096(-05)
July								
5	5.062(+00)	7.640(-03)	5.368(-05)	-2.070(-09)	3.662(-04)	8.820(-03)	2.728(-05)	1.901(-07)
15	5.705(+00)	1.245(-01)	4.551(-04)	-2.370(-07)	3.417(-02)	1.125(-02)	4.450(-04)	1.710(-06)
22	6.739(+00)	1.825(+00)	-4.879(-03)	6.163(-06)	9.216(-01)	1.515(-02)	6.616(-03)	3.679(-06)
30	9.230(+00)	4.455(-01)	1.555(-03)	-3.130(-06)	3.457(-01)	2.472(-02)	1.612(-03)	6.840(-06)

a more stable atmospheric brightness temperature. By the Kolmogorov's atmospheric turbulence model, the brightness fluctuations are characterised by a steep spectrum over a wide range of spatial frequencies, and the overall variance is dominated by the largest scales. For the wind speed of the order  $O(1)$  m/s typical for a calm sky without frontal activities, 1-hour time scale corresponds to  $L \sim O(10)$  km length scales, which coincide with the largest scales from the inertial sub-range, in which the atmospheric turbulence driven cascade of kinetic energy transport takes place. Incidentally, this rough estimate remains in agreement with theoretical predictions from the atmospheric turbulence model (Baars 2007), which for the same frequency at the sea level gives  $\Delta T_{\text{atm}} \approx 0.0055 T_{\text{atm}}$ , that is  $\Delta T_{\text{atm}} \approx \{0.06, 0.11\}$  K at 30 GHz for January and July respectively (Table 3). This is also qualitatively compatible with an independent analysis involving the near-ground RH variability and wind speed measurements (Lew 2016, in preparation).

#### 4.5 Accuracy limits

The precision to constrain the local, mean  $T_{\text{atm}}$  and  $\tau$  range from  $\sim 0.2\%$  at 5 GHz to  $\sim 13\%$  at 22 GHz (see Table 3 for January). These uncertainties refer to the monthly mean estimates, rather than to individual PWV measurements, although the dispersion of the individual measurements affects the  $\chi^2$  value when model fitting. A random PWV measurement may deviate significantly from the mean even in clear sky conditions (e.g. see the scatter from individual PWV measurements in Fig. 5 or Table 1). In order to assess the accuracy with which the actual  $T_{\text{atm}}$  and  $\tau$  can be constrained from the statistical analysis of the climatology data, we calculate the impact of the greatest variations, observed in our PWV measurements, on the values of  $T_{\text{atm}}$  and  $\tau$ .

The greatest observed variation of PWV in our sample occurs in June (Table 1) and ranges from  $w \sim 9$  mm to  $w \sim 23$  mm and the  $1\sigma$  variation is approximately  $\pm 6.1$  mm. Assuming linearity of the PWV- $T_{\text{atm}}$  relation ( $a_1$  coefficients for July in Table 4), this translates to  $1\sigma$  temperature variations  $\Delta T_{\text{atm}} \lesssim \pm \{0.05, 0.8, 11, 2.7\}$  K at  $\nu = \{5, 15, 22, 30\}$

from a single day observations in January and July, but the amplitude depends on the considered time-scale, and also somewhat varies from one day to another.

GHz, or by about  $\Delta T_{\text{atm}}/T_{\text{atm}} \approx \pm \{1, 9, 26, 14\} \%$  (see Table 3 for July). Clearly, low frequencies are the least sensitive to WV variations, as expected.

#### 4.6 Clear sky detection

By the analysis of the ground-level solar irradiance ( $E_{\odot}$ ), temperature ( $T$ ) and all-sky images, we observe that in clear sky conditions there is a good positive correlation between the solar irradiance and air temperature. At such times  $E_{\odot}$  and  $T$  are smooth functions of time. On the other hand, clouds passing through the LOS towards the Sun generate a high frequency noise (Fig. 13 second row panels). We anticipate that this feature can be used for automatic cloud detection in meteorological data analyses, but we defer details to a separate study.

In Sec. 1 we mentioned that for a fixed pressure level the RH has a diurnal variation corresponding to temperature variations of the atmospheric layer. The RH variation anti-correlates with the near-ground atmospheric temperature and also with the solar irradiance (Fig. 13) detected at DMC. However, IGRA data from Legionowo (Sec. 2.2.1) are recorded only twice a day (midday and midnight) and it is impossible to analyse the stability of diurnal variations of RH in an attempt to infer the cloud cover. It is therefore, interesting to see how feasible it is to select sub-samples of IGRA data, that would statistically correspond to clear sky conditions, given only few observational parameters:  $T, P$  and  $T_{\text{dew}}$ . We will investigate this using local sky images archived at DMC and  $T, P$  and RH measurements from TCfA, coarse averaged at 1-hour time scale. The distance between the two sites is  $\sim 8$  km.

The amplitude of diurnal temperature variations is the greatest in clear sky conditions. This is because the radiative cooling of the surface of the Earth is more efficient without heat-trapping clouds. Since the RH follows these variabilities in anti-phase, it should be expected that at fixed temperatures a selection based on the lowest daytime RH values should statistically correspond to clear sky conditions. On the other hand, a thick cloud cover tends to mitigate the amplitude of day to night variations in temperature and humidity. In this section we report results of a statistical analysis aimed to verify the accuracy of this hypothesis.

The hourly averaged ground-level meteorological data (Sec. 2.4) are screened by RH to form a sub-sample of the

**Table 5.** Summary of the sensitivity of the cloud detection algorithm by low ground-level RH values for the two cloud cover categories: ‘All’ where all types of clouds are considered, and ‘Low and Medium’ for which high clouds are treated as a clear sky.

Cloud cover sky fraction (CI <sup>c</sup> )	Clouds <sup>a</sup> : Season <sup>b</sup> :	True-Positive fraction [%]					
		All			Low & Med.		
		C&H	C	H	C&H	C	H
≤ 0.125 (1)		24	23	24	57	56	58
≤ 0.250 (2)		34	29	40	65	56	74
≤ 0.375 (3)		48	35	62	76	62	89

<sup>a</sup>Type of clouds considered. ‘Low & Med.’ means that all high clouds (if present) were treated as a clear sky.

<sup>b</sup>‘H’ - hot season: months from April to September, ‘C’ - cold season: months from October to March, ‘C&H’ - all year.

<sup>c</sup>CI - cloud cover index ranging from 0 to 8. For example, CI = 1 corresponds to cloud cover sky fraction of  $1/8 = 0.125$ .

5% driest conditions (sec. 2.4). In order to mitigate effects of diurnal temperature variations we consider only the samples obtained between hours 10:00 and 14:00 of the UTC+1 time. Such a choice roughly corresponds to the times when the temperatures should be the most stable (Fig. 13). The selection typically picks out two days per each month, depending on data completeness. Next, we visually analyse the all-sky images for the selected days and times and assign a mean cloud cover index for two cases: (i) disregarding the distinction between high, medium and low clouds, and (ii) ignoring high clouds i.e. treating them as clear sky. The cloud cover index (CI) can range from 0 for no clouds situation, up to 8 for the full sky cloud cover. We disregard whether the cloud cover is thin or thick, which is a conservative choice. The result is summarised in Table 5

Clearly, the selection by RH at the ground level has a high false-positive (low true-positive) fraction when all types of clouds are considered (see ‘All’ column in Table 5). However the situation significantly improves when high clouds are treated as a clear sky. This result is easy to interpret. There is generally a poor correlation between RHs (or the corresponding H<sub>2</sub>O VMRs) at different pressure levels (altitudes) hence, there is no guarantee that selection by low near-ground RHs will pick out days with no or little high cloud cover. Even the straightest selection by RH (5% driest days per month) does not always select fully cloudless days. This typically happens for the months during which the sky is cloudy most of the time (such as November in Poland). An example of a false-positive detection is shown in Fig. 13. The two days were selected by the algorithm as cloudless. The RH variabilities (bottom panels) and their lowest values are similar in both cases. Yet, a visual inspection revealed that the earlier day was contaminated by high clouds and classified as CI = 6 on the average, as opposed to the latter day classified with CI = 0. It seems however, that solar irradiance measured directly to the Sun could be effectively used to detect clouds by analysing the high frequency Fourier modes of the time domain signal.<sup>12</sup> When

<sup>12</sup> We measure the solar irradiance using the *CMP22* pyranometer operating in the spectral range from 200 nm to 3600 nm and within ~ 180° FOV.

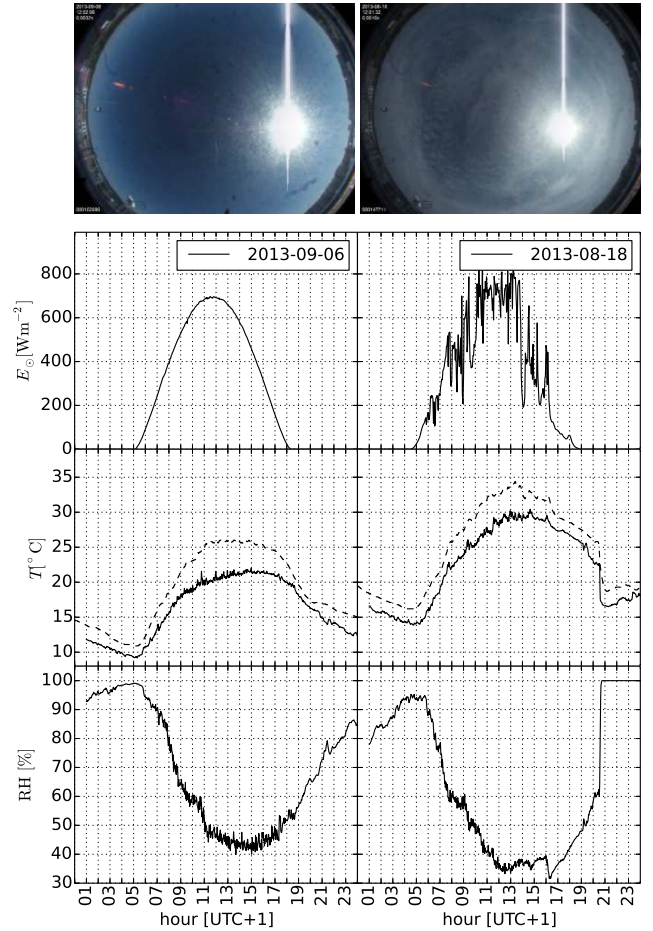


**Figure 13.** Comparison of atmospheric parameters on two different days identified as having clear sky conditions, selected on the basis of low RH values. The left panels show the correct selection (with an average 4-hour cloud cover CI = 0), and the right panels show an example of a false-positive selection (with an average 4-hour cloud cover CI ≈ 6). From the top to the bottom the panels show the all-sky camera picture around noon (UTC+1), the ground-level all-sky solar irradiance, temperature and RH. The dashed lines trace the *CMP 22* pyranometer sensor temperature. While the false-positive selection occurred most likely due to the little impact of high clouds on the near-ground RH, the impact of such a thin layer of high clouds is clearly significant on the detected irradiance.

treating high clouds as clear sky, however, the selection of days with cloud cover below 0.375 is accurate in ~ 76% of cases year-round and in ~ 89% of cases during the hot season (see Table 5). We have not investigated the specificity of the estimator – i.e. we have not estimated the fraction of clear sky days that eluded detection, but we are aware of such cases.

On average, disregarding the cloud type, the fraction of days with cloud cover ≤ 20% is ~ 10% year-round, ~ 12% in the hot season<sup>13</sup> and ~ 8% in the cold season for the RT32 region (Woś 2010). Based on the data from Table 5 (interpolated for the cloud cover ≤ 20%), in the case of all

<sup>13</sup> See Table 5 for the definitions of the hot and cold seasons.

types of clouds, using a binomial distribution with the number of trials fixed by the number of clear sky day candidates selected by the algorithm, we estimate that the probability of obtaining the reported true-positive rates by chance is very low,  $< 10^{-4}$ . Here, we assumed a true-positive outcome as a successful trial, with the probability defined by the aforementioned cloud cover statistics established by the local climate.

While the algorithm of selecting clear sky conditions by low, ground-level RHs yields a statistically significant result, we have not investigated the true-positive fractions where only a single measurement per day is available (case for IGRA data). It is possible however, that the algorithm can be improved by modifying the time range for data selection (here set between 10:00 and 14:00 of UTC+1), or by altering the RH threshold (here set at 5% of driest conditions), or by including the long-term pressure variations. Due to the reasons described in Sec. 2.5, for the main analysis, we employed external PWV measurements to match the data selection criteria to the clear sky requirements.

## 5 DISCUSSION

We used PWV observations (Sec. 2.6) to match the mean PWV profile from the sounding data (Sec. 2.2) to the expectations of clear sky conditions. With the current parametrisation (Sec. 2.5), however, we are unable to relate the  $p_H$  best fit value to some other observational quantity that is known from meteorological statistics, hence the constrained value of the  $p_H$  selection parameter is potentially useful only for the locations with similar climate. Where local clear sky PWV measurements are not available, a reasonable approximation of the clear-sky atmospheric WV profile could be found using the nearest AERONET data (Sec. 4.1, Fig. 5 and Fig. 6).

Although filtering meteorological data by the lowest 5% of the ground-level RH, statistically, tends to pick up cloudless days (Sec. 4.6 and Table 5), such a single level selection does not correspond to the 0.05 value of the  $p_H$  selection parameter since, by definition,  $p_H$  filters the data coherently at all altitudes (Sec. 2.5), therefore such an association would strongly bias the statistics towards the driest conditions.

## 6 CONCLUSIONS

We use climatological data to reconstruct the vertical structure of the atmosphere, constrain month-dependent profiles of precipitable water vapour (PWV), and predict the atmospheric brightness temperature ( $T_{\text{atm}}$ ) and optical depth ( $\tau$ ) at cm-wavelengths. We demonstrate that the nearly global coverage of the publicly available climatological data enables investigation of almost every location world wide, with the spatial resolution of a few hundred kilometres, on average (Sec. 2).

We compare the month-dependence of the column PWV, reconstructed for the location of the 32-metre radio telescope (RT32) located near Toruń (Poland), with the AERONET data, collected at the closest station located in Belsk. We find that the two are closely correlated throughout the year, which supports the reliability of the PWV re-

construction from sounding and ground-base meteorological data.

Bearing in mind the prerequisites of radio source continuum flux density measurements at cm-wavelengths, we focus on radiative properties of the atmosphere in clear sky conditions. We present a compilation of  $\sim 17$  months of local PWV observations collected in clear sky conditions using the MICROTOPS II sun photometer (Sec. 4.1). We use these observations to devise a selection criterion, which when applied to the climatological data, enables us to reconstruct the vertical structure of the atmosphere that is compatible with a cloudless sky.

Using the reconstructed clear sky PWV profile, and solutions of the radiative transfer through the atmosphere, we constrain  $T_{\text{atm}}$  and  $\tau$  for the first time for the location of RT32 (Sec. 4.2). We also establish PWV- $T_{\text{atm}}$  and PWV- $\tau$  scaling relations (Sec. 4.4) that can be used to constrain atmospheric brightness temperature and optical depth in clear sky conditions, given an independent estimate of PWV (e.g. from a local GPS station). We estimate that in clear sky conditions, the mean monthly values of  $T_{\text{atm}}$  and  $\tau$ , inferred from climatology data, constrain the actual values to within  $\pm\{1, 9, 26, 14\}$  % (at  $1\sigma$  CL) at  $\nu = \{5, 15, 22, 30\}$  GHz. These estimates should also apply to other locations at similar latitudes and a compatible climate (Sec. 4.5).

We calculate the zenith distance ( $z_d$ ) dependence of  $T_{\text{atm}}$  and discuss  $\lesssim 10\%$  effects regarding radio-source continuum flux density measurement calibrations. We discuss the implications of using optically thin, single-layer, and flat atmosphere approximations in determining the optical depth and estimating corrections for atmospheric absorption (Sec. 4.3.4). For the selected frequencies, we quantify deviations of  $T_{\text{atm}}(z_d)$  and  $\tau(z_d)$  from a simple geometrical scaling  $\sim \sec(z_d)$  in the case of non-planar atmosphere. We also constrain the physical temperature of the multi-layer atmosphere by introducing a single-layer equivalent temperature, which we next connect to the local ground level temperatures by a simple relation (Sec. 4.3). The connection should be readily useful when constraining atmospheric optical depth due to absorption and scattering.

Finally, we discuss the sensitivity of a clear sky selection criterion involving ground-level relative humidity (RH). This criterion can be used to detect cloudless days from data that only contain measurements of a few basic atmospheric parameters, such as temperature, pressure and dew point, which are typically collected by weather balloons and ground meteorological stations. By the analysis of archival all-sky images, we find that for any given month selecting meteorological data by the lowest daytime RH can correctly identify days with a mean cloud cover below  $\sim 0.38$  in 48% of cases, if one disregards whether the sky is obscured by low, medium or high level clouds, and in 76% of cases if only low and medium level clouds are considered. We find that reproducing these true-positive fractions by chance is unlikely at odds greater than  $10^4 : 1$  taking into account the local probability of cloudless skies, and the number of days used for the analysis (Sec. 4.6). We find that the effectiveness of the estimator is increased during the hot season (April–September) when the true-positive fraction among the clear-sky days selected by this algorithm reaches  $\sim 89\%$  (for the case when high level clouds are treated as a clear sky). We suspect that

the effectiveness of this estimator should be similar in other locations with a compatible climate.

## ACKNOWLEDGEMENTS

BL would like to thank Mike Peel and Marcin Gawroński for useful discussions on observational pipelines used in OCRA observations. Also thanks to Scott Paine for comments on PWV- $\tau$  scaling relations. Thank you to Peter Wilkinson for comments on the early version of the manuscript, and to Boud Roukema and to the anonymous referee for their useful comments and suggestions.

Use was made of data from the Global Climatology of Atmospheric Parameters from the Committee on Space Research (COSPAR) International Reference Atmosphere (CIRA-86) Project. We acknowledge the use of Integrated Global Radiosonde Archive (IGRA) data from the Legionowo station. The data was also sourced from the Canadian Atmospheric Chemistry Experiment. We thank Piotr Sobolewski, Brent Holben and Aleksander Pietruczuk for their effort in establishing and maintaining the Belsk AERONET station. This research has made use of the AM program (version 7.2) – a publicly-available tool for radiative transfer computations at microwave to submillimeter wavelengths, developed at the Harvard-Smithsonian Center for Astrophysics. We also acknowledge use of the 'matplotlib' plotting library (Hunter 2007).

This work was financially supported by the Polish National Science Centre through grant DEC-2011/03/D/ST9/03373. A part of this project benefited from the EC RadioNet FP7 Joint Research Activity “APRICOT” (All Purpose Radio Imaging Cameras On Telescopes).

## REFERENCES

- Ajello C., Bonelli G., Sironi G., 1995, *ApJS*, **96**, 643  
 Akima H., 1970, *JACM*, **17**, 589  
 Alduchov O., Eskridge R., 1997, *J. Appl. Meteor.*, **35**, 601  
 Baars J. W. M., 2007, *The Paraboloidal Reflector Antenna In Radio Astronomy And Communication Theory And Practice*. Springer New York  
 Bernath P. F., et al., 2005, *Geophys. Res. Lett.*, **32**, 15  
 Bussmann R. S., Holzappel W. L., Kuo C. L., 2005, *ApJ*, **622**, 1343  
 Bustos R., Rubio M., Otárola A., Nagar N., 2014, *PASP*, **126**, 1126  
 Durre I., Vose R. S., Wuertz D. B., 2006, *J. Climate*, **19**, 53  
 Fioletov V. E., Bodeker G. E., Miller A. J., McPeters R. D., Stolarski R., 2002, *J. Geophys. Res.*, **107**, 4647  
 Fixsen D. J., 2009, *ApJ*, **707**, 916  
 Gawroński M. P., et al., 2010, *MNRAS*, **406**, 1853  
 Hardy B., 1998, *Proceedings in Third International Symposium on Humidity and Moisture*, **1**, 214  
 Hunter J. D., 2007, *Computing In Science & Engineering*, **9**, 90  
 Jones A., et al., 2012, *Atmospheric Chemistry and Physics*, **12**, 5207  
 Lancaster K., et al., 2011, *MNRAS*, **418**, 1441  
 Lawrence M. G., 2005, *Bull. Amer. Meteor. Soc.*, **86**, 225  
 Lew B., Birkinshaw M., Wilkinson P., Kus A., 2015, *J. Cosmology Astropart. Phys.*, **2**, 4  
 Liljegren J. C., Clothiaux E. E., Mace G. G., Kato S., Dong X., 2001, *J. Geophys. Res.*, **106**, 14485  
 Murphy D. M., Koop T., 2005, *Q. J. R. Meteorol. Soc.*, **131**, 1539  
 NASA 1976, Technical report, U.S. Standard Atmosphere, 1976. U.S. Government Printing Office Washington, D.C.  
 Paine S., 2012, Smithsonian Astrophysical Observatory, SMA technical memo 152 v.7.2  
 Paine S., 2015, private communication  
 Paul J., Fortuin F., Kelder H., 1998, *J. Geophys. Res.*, **103**, 31709  
 Peel M., 2010, preprint, ([arXiv:1006.2760](https://arxiv.org/abs/1006.2760))  
 Peixoto J., Oort A. H., 1996, *J. Climate*, **9**, 3443  
 Radford S. J., Holdaway M. A., 1998, in Phillips T. G., ed., *Society of Photo-Optical Instrumentation Engineers (SPIE) Conference Series Vol. 3357, Advanced Technology MMW, Radio, and Terahertz Telescopes*. pp 486–494  
 Rees D., 1988, *Advances in Space Research*, **8**  
 Rees D., 1992, *Planet. Space Sci.*, **40**, 555  
 Rees D., Barnett J. J., Labitzke K., 1990, *Advances in Space Research*, **10**  
 Schoenberg E., 1929, "Theoretische Photometrie" in *Hdb. d. Astrophys.* Bd. II/1  
 Smirnov A., Holben B., Eck T., Dubovik O., Slutsker I., 2000, *Remote Sensing of Environment*, **73**, 337  
 Soden B. J., Lanzante J. R., 1996, *J. Climate*, **9**, 1235  
 Sonntag D., 1990, *Z. Meteorol.*, **40**, 340  
 WOUDC 1961, *World Ozone and Ultraviolet Radiation Data Centre*, p. <http://www.woudc.org>  
 Wilson T. L., Rohlf K., Hüttemeister S., 2009, *Tools of Radio Astronomy*. Springer-Verlag, [doi:10.1007/978-3-540-85122-6](https://doi.org/10.1007/978-3-540-85122-6)  
 Woś A., 2010, *Klimat Polski w drugiej połowie XX wieku*. Wydawnictwo Naukowe UAM

This paper has been typeset from a  $\text{\TeX}/\text{\LaTeX}$  file prepared by the author.